A Comprehensive Review of Electric Solar Wind Sail Concept and its Applications

Marco Bassetto, Lorenzo Niccolai, Alessandro A. Quarta*, Giovanni Mengali

Department of Civil and Industrial Engineering, University of Pisa, I-56122, Italy

Abstract

The Electric Solar Wind Sail (E-sail) is an innovative propellantless propulsion system conceived by Pekka Janhunen in 2004 for use in interplanetary space. An E-sail consists of a network of electrically charged tethers maintained at a high voltage level by an electron emitter. The electrostatic field surrounding the E-sail extracts momentum from the incoming solar wind ions, thus giving rise to the generation of a continuous thrust. In a geocentric context, the same physical principle is also exploited by the plasma brake, a promising option for reducing the decay time of satellites in low Earth orbits after the end of their operational life. This paper discusses the scientific advances of both E-sail and plasma brake concepts from their first design to the current state of the art. A general description of the E-sail architecture is first presented with particular emphasis on the proposed tether deployment mechanisms and thermo-structural analyses that have been carried out over the recent years. The working principle of an E-sail is then illustrated and the evolution of the thrust and torque vector models is retraced to emphasize the subsequent refinements that these models have encountered. The dynamic behaviour of an E-sail is also analyzed by illustrating the mathematical tools that have been proposed and developed for both orbital dynamics and attitude control. A particular effort is devoted to reviewing the numerous mission scenarios that have been studied to date. In fact, the extensive literature about E-sail-based mission scenarios demonstrates the versatility of such an innovative propulsion system in an interplanetary framework. Credit is given to the very recent studies on environmental uncertainties, which highlight the importance of using suitable control strategies for the compensation of solar wind fluctuations. Finally, the applications of the plasma brake are thoroughly reviewed.

Keywords: Electric solar wind sail, plasma brake , Coulomb drag , propellantless propulsion system, spacecraft mission design

Nomenclature

A	=	spacecraft conductive area, [m^2]
$\mathbb{A}$	=	state matrix
$\boldsymbol{a}$	=	propulsive acceleration vector (with $\hat{\boldsymbol{a}} \triangleq \boldsymbol{a}/\left\|\boldsymbol{a}\right\|$), [$\mathrm{mm/s}^2$]
a	=	semimajor axis, [au]
a_c	=	characteristic acceleration, [$\mathrm{mm/s}^2$]
a_r	=	radial component of propulsive acceleration, [$\mathrm{mm/s}^2$]
a_n	=	normal component of propulsive acceleration, [$\mathrm{mm/s}^2$]
a_t	=	transverse component of propulsive acceleration, [$\mathrm{mm/s}^2$]
b_i	=	best-fit coefficients of α, see Eq. (5)

*Corresponding author

Email addresses: marco.bassetto@ing.unipi.it (Marco Bassetto), lorenzo.niccolai@ing.unipi.it (Lorenzo Niccolai), a.quarta@ing.unipi.it (Alessandro A. Quarta), g.mengali@ing.unipi.it (Giovanni Mengali)

Published in Progress in Aerospace Sciences, Vol. 128 January 2022, pp. 100768 (1–27). doi: https://doi.org/10.1016/j.paerosci.2021.100768

b_t	=	tether width, [mm]
$\boldsymbol{c}$	=	auxiliary vector, see Eq. (4.1)
$\{C_1,\, C_2\}$	=	constants of integration, see Eqs. (43)-(44)
c_i	=	best-fit coefficients of γ, see Eq. (6)
D	=	Coulomb drag, [N]
d	=	auxiliary coefficient, see Eq. (7)
e	=	eccentricity
e_e	=	elementary charge, [C]
$\{\hat{\boldsymbol{e}}_r,\, \hat{\boldsymbol{e}}_t,\, \hat{\boldsymbol{e}}_n\}$	=	unit vectors of $\mathcal{T}_{\rm RTN}$
$\boldsymbol{F}$	=	E-sail thrust vector (with $F \triangleq \|\boldsymbol{F}\|$), [N]
$\{f_1,\, f_2,\, f_3\}$	=	functions of $\{n,\, v_{\rm rel}\}$, see Eq. (56)
g_0	=	standard gravity, [m/s^2]
H	=	spacecraft altitude, [km]
$\mathcal{H}$	=	Hamiltonian function
I_e	=	negative current collected by the spacecraft, [A]
I_i	=	ion current gathered by the generic tether, [A]
I_t	=	transverse moment of inertia, [kg m^2]
I_z	=	longitudinal moment of inertia, [kg m^2]
i	=	inclination
$\{\hat{\boldsymbol{i}}_B,\, \hat{\boldsymbol{j}}_B,\, \hat{\boldsymbol{k}}_B\}$	=	unit vectors of $\mathcal{T}_B$
$\{\hat{\boldsymbol{i}}_I,\, \hat{\boldsymbol{j}}_I,\, \hat{\boldsymbol{k}}_I\}$	=	unit vectors of $\mathcal{T}_I$
k_B	=	Boltzmann constant, [J/K]
$k_{\text{œ}}$	=	functions of e and ν, see Eqs. (37)–(40)
K_t	=	multiline tether coefficient, see Eqs. (3) and (50)
$\mathcal{L}$	=	tether length, [m]
$\mathcal{M}$	=	shape coefficient, see Eq. (15)
m	=	total spacecraft mass, [kg]
m_e	=	electron mass, [kg]
m_i	=	ion mass, [kg]
m_p	=	proton mass, [kg]
$m_{\rm PB}$	=	total plasma brake system mass, [g]
N	=	number of tethers
$\hat{\boldsymbol{n}}$	=	unit vector normal to the sail plane
n	=	plasma density, [m^{-3}]
œ	=	generic classical orbital element
P	=	power consumption, [W]
$\mathcal{P}$	=	shape coefficient, see Eq. (11)
$\{p,\, f,\, g,\, h,\, k,\, L\}$	=	Modified Equinoctial Orbital Elements
q	=	ratio of p to r
R	=	auxiliary coefficient, see Eq. (7)
$R_\oplus$	=	Earth's equatorial radius, [km]
$\boldsymbol{r}$	=	spacecraft position vector (with $\hat{\boldsymbol{r}} \triangleq \boldsymbol{r}/\,\|\boldsymbol{r}\|$), [au]
r	=	orbital radius, [au]
r_w	=	wire radius, (μm)
$r_\oplus$	=	reference distance (1 au)
s	=	tether shape function, [m]
S	=	spacecraft center of mass
t	=	time, [s]
$\boldsymbol{T}$	=	E-sail torque vector, [Nm]
T	=	particle temperature, [K]
T_e	=	electron temperature, [K]
T_i	=	ion temperature, [K]
$\hat{\boldsymbol{t}}$	=	transverse unit vector
$\mathcal{T}_B$	=	body reference frame

$\mathcal{T}_I$	=	inertial reference frame
$\mathcal{T}_{\rm RTN}$	=	radial-transverse-normal reference frame
V	=	electric potential, [V]
$V^\star$	=	modified electric potential, see Eq.(53), [V]
$\boldsymbol{v}$	=	spacecraft velocity vector (with $v \triangleq \|\boldsymbol{v}\|$), [km/s]
v_r	=	radial velocity, [km/s]
$v_{\rm sw}$	=	solar wind speed, [km/s]
$v_{\rm rel}$	=	spacecraft speed relative to ionosphere, [km/s]
v_φ	=	circumferential velocity, [km/s]
x	=	abscissa, [m]
x_t	=	distance between tether tip and sail spin axis, [m]
$\boldsymbol{x}$	=	state vector
α	=	thrust cone angle, [rad]
α_n	=	sail pitch angle, [rad]
β	=	exponent, see Eq. (41)
γ	=	dimensionless propulsive acceleration, see Eq. (6)
δ	=	clock angle, [rad]
ϵ_0	=	vacuum permittivity, [C/V]
η	=	payload mass fraction
κ	=	mass-to-power ratio
$\boldsymbol{\lambda}$	=	costate vector
$\{\lambda_p, \lambda_f, \lambda_g, \lambda_h, \lambda_k, \lambda_L\}$	=	components of $\boldsymbol{\lambda}$
λ_{De}	=	Debye length, [m]
$\mu_\odot$	=	Sun's gravitational parameter, [$\rm km^3/s^2$]
ν	=	true anomaly, [rad]
ρ_w	=	wire density, [$\rm kg/m^3$]
τ	=	switching parameter
φ	=	polar angle, [rad]
$\{\phi, \theta, \psi\}$	=	Euler's angles, [rad]
ω	=	argument of periapsis, [rad]
$\boldsymbol{\Omega}$	=	spacecraft angular velocity, [rad/s]
Ω	=	right ascension of the ascending node, [rad]
$\{\Omega_x, \Omega_y, \Omega_z\}$	=	components of $\boldsymbol{\Omega}$ in $\mathcal{T}_B$, [rad/s]

Subscripts

f	=	final
j	=	time step of the simulation
max	=	maximum
st	=	maximum allowable voltage variation
t	=	relative to a single tether
0	=	initial
$\wedge$	=	unit vector
$\oplus$	=	evaluated at $r = r_\oplus$

Superscripts

eff	=	effective
$\cdot$	=	time derivative
$'$	=	derivative w.r.t. x
$\sim$	=	reference value

1. Introduction

Space missions are traditionally based on propulsion technologies that allow the spacecraft thrust to be generated by consuming a certain amount of propellant. Of course, the required propellant must be

stored onboard and, as such, it contributes to increasing both the total spacecraft mass and the overall mission costs. Moreover, the need for propellant on board limits the mission lifetime since an adequate orbital maintenance usually requires corrective maneuvers that are impossible to do when propellant is no longer available. Another limit is related to the impossibility of traditional chemical thrusters to generate a continuous thrust acting for long times, which is indispensable for carrying out some advanced mission scenarios.

In the last decades, some new propellantless propulsion technologies have been proposed to overcome these limitations. The first and more relevant example is represented by solar sails [1, 2, 3], which exploit the solar radiation pressure acting on a thin reflective membrane to generate thrust. Recent solar sail-based missions, such as IKAROS [4] or LightSail-2 [5], have successfully flown demonstrating the potentialities of solar sail technology. Another interesting example is constituted by the magnetic sail concept proposed by Zubrin and Andrews [6, 7, 8, 9], which makes use of a magnetic bubble to deflect the solar wind ions and extract momentum from them. This concept has been later investigated and extended by other authors [10, 11, 12, 13, 14, 15, 16] but, unfortunately, no *in-situ* test of the magnetic sail technology has been attempted so far. A further propellantless technology that may be applied to geocentric scenarios is the electrodynamic tether [17, 18], which produces a drag due to the Lorentz force generated by the interaction between a current flowing in a tether and the Earth's magnetosphere.

The most recently proposed propellantless propulsion technology is the Electric Solar Wind Sail (shortened with electric sail or E-sail), which was first conceived by Janhunen in 2004 [19]; see Fig. 1. In its original

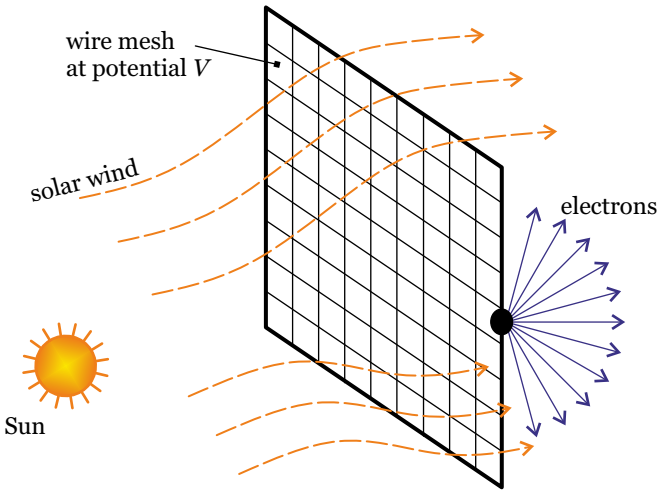

Figure 1: Original E-sail arrangement as wire mesh. Adapted from Ref. [19].

concept, an E-sail is a large grid of tethers maintained at a high positive electrical voltage; see Fig. 1. When immersed in the solar wind plasma, the grid of tethers generates a thrust by extracting momentum form the ions. The working principle of an E-sail is therefore similar to that of other propellantless propulsion systems [20, 21], but it is based on an electrostatic interaction between the plasma flow and the artificial electric field surrounding the E-sail.

From the first E-sail concept described in the pioneering paper by Janhunen [19], the potentialities of this advanced technology, along with the main associated issues, have been deeply investigated by many research groups and space agencies [22, 23, 24]. Currently, the typical E-sail configuration consists of long conductive tethers, arranged in a radial pattern so as to form a sort of spoked wheel, which are stretched out by the centrifugal force due to the spacecraft spin. The tethers are kept at a high positive potential by means of an electron gun, which expels the electrons attracted by the positively biased tethers; see Fig. 2.

The aim of this paper is to provide a systematic and thoroughly review of the several aspects associated with the E-sail. More precisely, Section 2 provides a general description of the E-sail concept, discusses the deployment strategies and the manufacturing processes, and provides a review of the structural analyses discussed in the recent literature. Then, Section 3 describes the tools used to model the thrust and torque

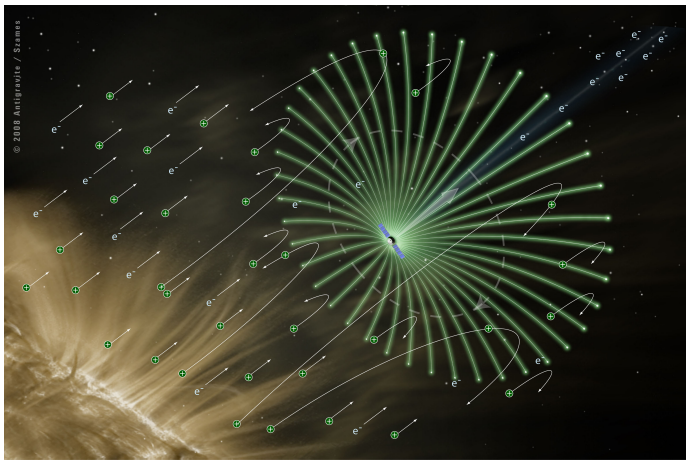

Figure 2: E-sail artistic rendering. Courtesy of Alexandre Szames, Antigravité (Paris).

vectors, while Section 4 applies the previous results to calculate the spacecraft trajectory and the E-sail attitude. Section 5 discusses the available control strategies to achieve an optimal propelled trajectory and a desired E-sail attitude. The potential heliocentric mission scenarios for an E-sail are described in Section 6, while a possible geocentric application of the E-sail working principle in a deorbiting scenario, the plasma brake, is thoroughly discussed in Section 7, along with the attempted experimental tests. Finally, the Conclusions resume the main outcomes of this review.

2. E-sail architecture

An E-sail generates thrust from the electrostatic interaction between the charged tethers and the ions in the solar wind plasma. The peculiar features of an E-sail are its lightness and the possibility of orienting the thrust vector, albeit within certain limits. These two advantages make the E-sail competitive with conventional thrusters or other propellantless propulsion systems (like solar sails), which, however, have greater technological maturity. This section reviews configurations, deployment mechanisms, manufacturing, materials, and thermo-structural analyses regarding the E-sail concept.

2.1. E-sail configurations

Depending on the mission requirements, an E-sail must be able to change its spatial orientation in order to adjust the direction of its thrust vector. This is possible by modulating the potential of each tether in a synchronous way with the sail rotation. In fact, the force acting on the generic tether depends on its electrical voltage. However, when performing an attitude variation, it is necessary to take into account that a transverse thrust component induces an angular velocity change of each tether [25]. Other phenomena, including Coriolis forces [26] and solar wind velocity fluctuations, generate similar effects [27]. A suitable E-sail configuration is therefore necessary for removing any difference in angular velocity between tethers and so avoiding possible tether collision. The requirement of lightweight is also essential for an E-sail since its propulsive acceleration is inversely proportional to the total spacecraft mass.

The typical arrangement of an E-sail consists of a number of thin, long, and electrically conductive tethers. The tethers are kept at a high positive potential by an onboard electron gun, which repels the negative charge from the system; see Fig. 3. Each tether tip hosts a remote unit, which is generally equipped with a small thruster with the aim of adjusting the E-sail spin rate [28]. The remote units are connected to the adjacent ones by auxiliary tethers in such a way as to form a circle centered at the spacecraft main body. This configuration is useful to stabilize the complex cable system [28]. The auxiliary tethers are usually assumed to be non-conductive, although Janhunen and Toivanen [29] suggested the possibility of using conductive auxiliary tethers in order to control the E-sail spin rate by modulating their electrical voltage.

Other options have been proposed in the literature to maintain the desired tether spin rate. In this regard, a more complex arrangement consists in the use of conductive auxiliary tethers and in the alternation of

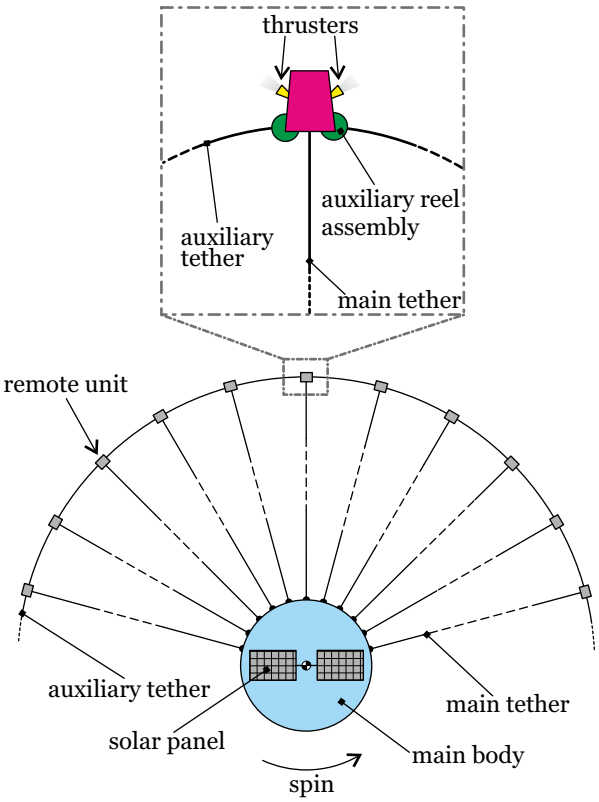

Figure 3: E-sail typical arrangement with remote units and auxiliary tethers. Adapted from Ref. [28].

main tethers connected to and insulated from the auxiliary ones. In particular, the tethers referred to as "T-tethers" are galvanically connected through the corresponding remote units with the two adjacent auxiliary tethers, while the those called "I-tethers" are insulated from the other parts of the rig; see Fig. 4. This architecture is denoted as "TI rig" and is discussed in Ref. [27] along with a control strategy of the tether voltages that allows for thrust vector modulation, spin rate control, tether oscillation suppression, and attitude variation. Janhunen and Toivanen [27] have shown that if the voltages of the auxiliary tethers can be controlled independently of the voltages of the main tethers, a spin rate control is possible while maintaining the orientation of the spin plane (i.e., the plane orthogonal to the spin axis). In particular, this is possible because one has two control parameters in each angular segment, that is, the main tether voltage and the auxiliary tether voltage.

Another possible E-sail configuration involves the use of photonic blades, similar to those of a heliogyro [30], which are located between the conductive tethers and the remote units and may be used to modify the E-sail spin rate [31, 32]; see Fig. 5. In that case, the photonic blades or the conductive auxiliary tethers significantly increase the system complexity and the deployment issues. Beyond all possible variants, the most commonly proposed E-sail architecture consists of a number of long main tethers arranged in a radial pattern. The tip of each main tether is equipped with a remote unit and is connected to the two adjacent main tethers by non-conductive auxiliary tethers; see Fig. 3.

It is easy to realize that the deployment of an E-sail with many long tethers represents a non-trivial problem (Section 2.2 is devoted to thoroughly discuss these issues). To overcome the obstacles imposed by the deployment of a so large structure, other simplified configurations have been proposed, which exploit the same working principle of a conventional E-sail. An example is the E-sail proposed in Ref. [33], which is made up of one or few charged tethers (see Fig. 6) and may be used as a propulsion system aboard nanosatellites in deep space. This configuration is also at the heart of the plasma brake concept to deorbit satellites from a low-Earth orbit (LEO); see Section 7.

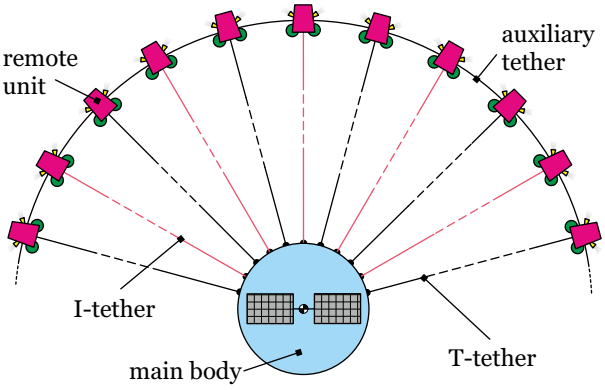

Figure 4: TI rig architecture. Adapted from Ref. [27].

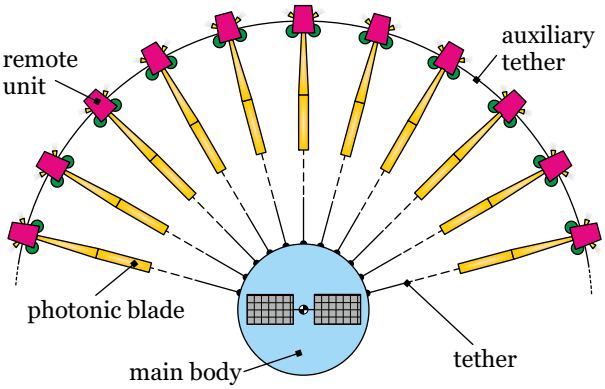

Figure 5: E-sail architecture with freely guided photonic blades. Adapted from Ref. [31].

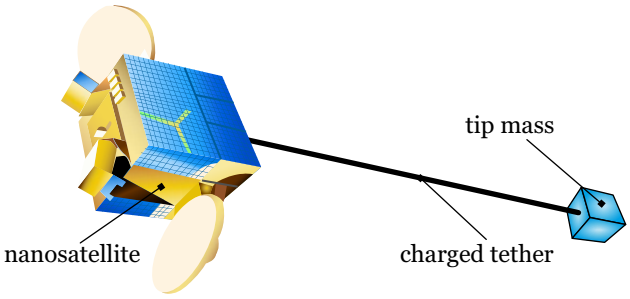

Figure 6: Single-tether E-sail-based nanosatellite conceptual scheme.

2.2. Deployment mechanisms

As previously discussed, a typical E-sail is made up of very long tethers. Such a large structure must be launched in a folded configuration in order to be packed inside the launch vehicle and then needs to be deployed in the deep space. Similarly to what happens for a classical solar sail, such an in-orbit deployment represents one of the most challenging phases of the whole mission due to the large inertia moments of the E-sail and the complex dynamics of the tethers during the deployment phase. However, although the deployment reliability is a critical issue to be addressed for a future E-sail mission, only few related works exist in the literature such as the interesting studies carried out by Fulton and Schaub [34, 35]. In these works, each tether has a tip mass and the E-sail is assumed to spin in the working configuration, which means

that the E-sail has a nonzero angular velocity at the end of its deployment phase. Each tether is modelled as a slender rod (i.e., its flexibility is neglected), thus greatly simplifying the problem. In particular, Fulton and Schaub [34, 35] proposed two possible deployment strategies, referred to as radial and a tangential deployment, which are sketched in Fig. 7.

The radial deployment strategy (see Fig. 7(b)) is based on the individual tether spooling concept and requires a dedicated tether reeling module and a drive mechanism to guide the radial deployment of each tether. The main advantage of this strategy is the possibility it offers to control each tether individually, thus reducing the risk of a general deployment failure. Each deployment unit acts as a single tether unreel mechanism, so that the complex deployment of the whole E-sail structure is decomposed into many simpler tether releases. However, the large number of actuators required by the radial deployment increases the total E-sail mass and its power consumption. Moreover, the numerical simulations discussed by Fulton and Schaub [35] highlight that the required spin rate is large and the deployment times are long.

An alternative is offered by the tangential deployment [35] (see Fig. 7(c)), where the tethers are initially deployed in the tangential direction and the tip mass of each tether acts like a classical yo-yo de-spinner mechanism. In practice, this method exploits the spacecraft spin motion to actuate the tether deployment. Initially, all tethers are wrapped around a central hub (i.e., the structure of the spacecraft main body). Then, they are released at the same time instant when the deployment phase begins. After the first unwrapping phase, when the whole length of each tether is fully released, the tethers pass from a tangential to a radial configuration through a hinging phase; see Fig. 7(d). According to the results presented in Ref. [35], the tangential deployment strategy is more complex to study due to the interaction between the spinning spacecraft and the tether dynamics, but it requires smaller spin rates and deployment times when compared to the radial deployment strategy. However, as the authors pointed out, the validity of the mathematical model used in Ref. [35] should be verified with a more accurate dynamical analysis, in which a lumped mass method is used to model the E-sail, in order to properly take into account the actual tether flexibility.

A first step in this sense is represented by the recent work of Li et al. [36], who included the tether flexility in the dynamical model as well as their kinematic coupling with the spacecraft rigid hub. The authors concentrated on a radial deployment strategy, and suggested using a proportional-derivative control law to achieve a given spin rate of the spacecraft body. Their results show that a radial deployment of a large E-sail structure requires a thrust with a nonzero tangential component to be provided by the remote units. In addition, the stability of the deployment is significantly affected by the thrust magnitude as well as by the deployment speed. Further analyses, theoretical investigations, and experimental tests are required to assess the feasibility of the proposed deployment strategies, which is still a significant issue to solve for the design of an E-sail-based space mission.

More recently, other mission concepts based on the E-sail working principle have been proposed, with either a single or few charged tethers only; see Section 7.2. In that case, the deployment phase is significantly simplified since a single unreel mechanism is sufficient to release the tether from the spacecraft hub. An example of tether unreel component is constituted by the WRECKER mechanism [37] (German acronym of "**W**eltraum Ab**r**ollm**ec**hanismus für dünnen ele**k**trisch leit**e**nden D**r**aht"), which was mounted on the ESTCube-1 nanosatellite and was supposed to deploy a plasma brake tether with an end mass and a length of 10 m; see Fig. 8. The WRECKER assembly was made of a tether reel, a drive mechanism with a piezoelectric motor, and two launch locks acting on the tether reel and on the end mass. Even though the WRECKER assembly did not survive the vibrational loads during the launch phase, its main features were used for the plasma brake experiment of Aalto-1 spacecraft, which is equipped with a total tether length of about 100 m. The unreel mechanism on board Aalto-1 is based on the same architecture as that of WRECKER, with small but significant improvements suggested by the WRECKER failure [38, 39]. The total mass of the system, which is composed of the tether and the unreel mechanism, is just 360 g. Further information on other planned missions involving plasma brake tethers or single-tether E-sails will be given in Section 7.2. The relatively simple design of the tether unreel mechanism is a strong advantage of these mission concepts, especially when compared to large E-sails to be deployed in the deep space.

2.3. E-sail structure and manufacturing

The tethers composing an E-sail must have a low density, a high electrical conductivity, and be able to withstand the deep space environment. The requirements on density and electrical conductivity have led to the choice of aluminum tethers. As for the problem of space survival, the most critical requirement is the

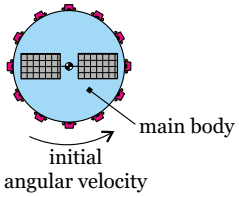

(a) Stowed condition.

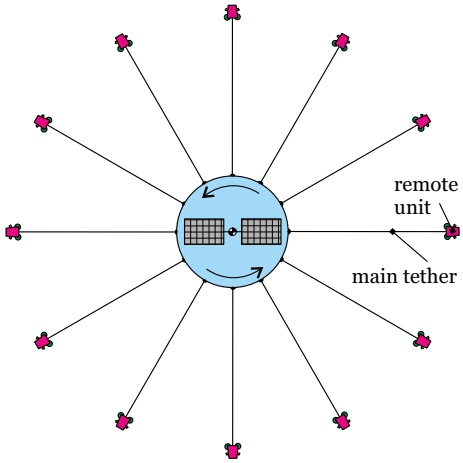

(b) Radial deployment scheme.

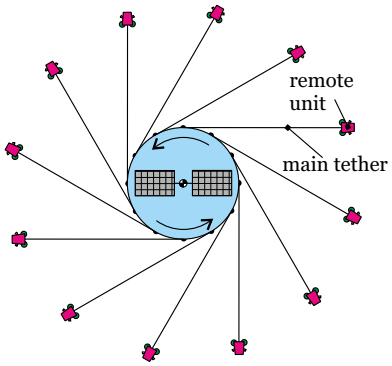

(c) Tangential deployment scheme.

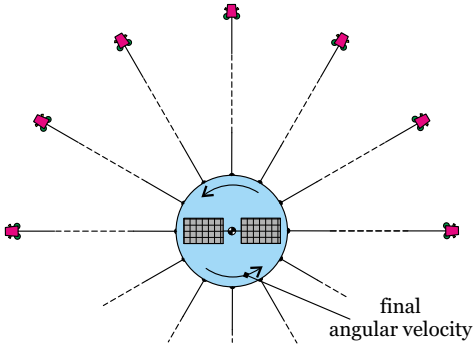

(d) Deployed condition.

Figure 7: Radial and tangential deployment strategies discussed in Refs. [34, 35].

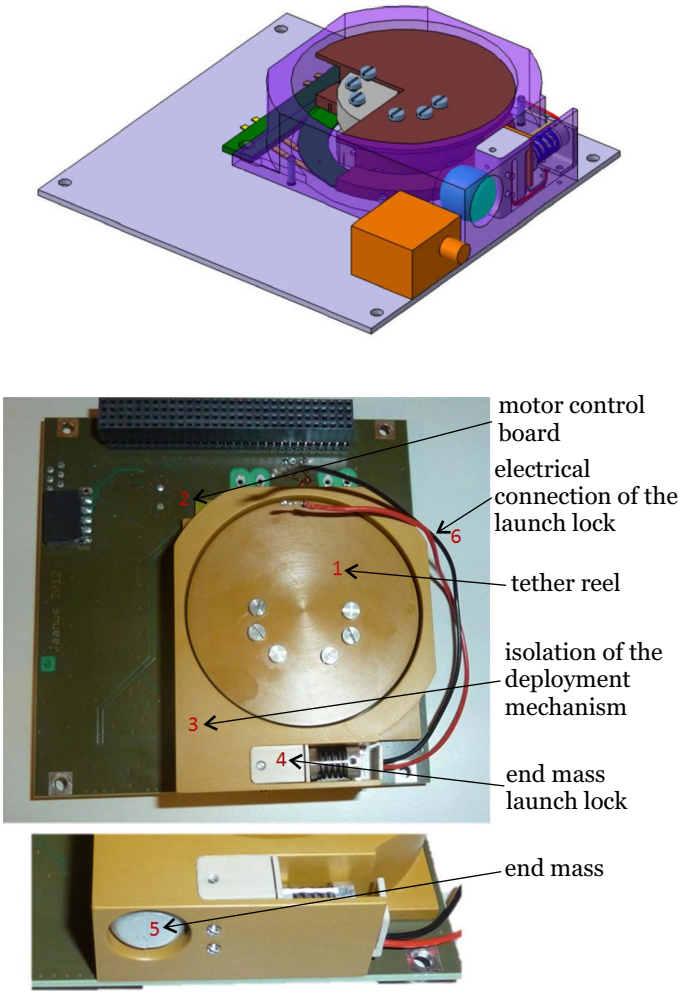

Figure 8: WRECKER mechanism: CAD and proto flight model. Adapted from Ref. [37], courtesy of the authors.

capability of cushioning impacts with small meteoroids without losing the conductive capability. To this end, the first proposed design for E-sail tethers was the Hoytether [40, 41] sketched in Fig. 9, which is made of two main lines (with a width of about $25 - 50\,\mu$m) with multiple interconnections made of smaller wires that guarantee an electric contact even in case of impact with a meteoroid. In fact, this feature increases the system lifetime compared to that of single line tether.

A recent innovation of the Hoytether concept is constituted by the Heytether [42], which is made of a single main line with multiple secondary interconnections, as shown in Fig. 10. This configuration guarantees a sufficient reliability, with lower total mass and design complexity than the Hoytether, and it is currently considered one of the best choices for E-sail arrangements; see Section 2.1.

The manufacturing of aluminum Heytethers requires the secondary interconnections to be bonded to the main tether, which may be obtained with ultrasonic bonding; see Fig. 11(a). These results were achieved within the European project EU ESAIL-FP7, lasted from 2007 to 2013, where the manufacturing of a kilometer long Heytether was analyzed; see Fig. 11(c). The outputs of the EU ESAIL-FP7 project, from the Heytethers manufacturing viewpoint, are summarized in Refs. [42, 43], which describe the method used for obtaining an automatic production of an Heytether structure with a velocity on the order of about 70 m/day. The encouraging results of the EU ESAIL-FP7 project suggested that the manufacturing of E-sail tethers is possible with the current technological level.

It is worth mentioning two additional tether structures, that is, those developed for the Coulomb drag propulsion aboard the ESTCube-2 and FORESAIL-1 satellites [44]. One of them, which is a multicell

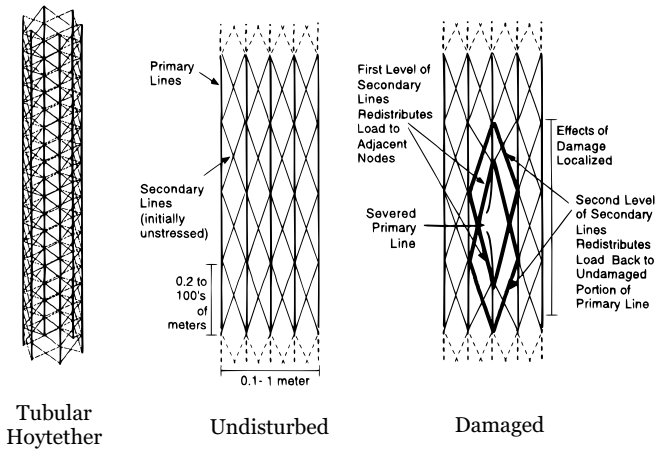

Figure 9: Hoytether scheme as introduced in Ref. [40]. Image courtesy of Robert Hoyt, Tethers Unlimited, Inc.

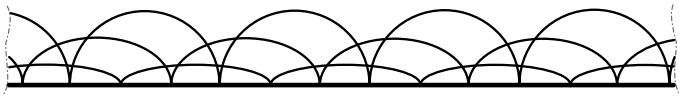

Figure 10: Basic sketch of a four-wire Heytether structure. Adapted from Ref. [28].

structure resembling a ladder, is based on the diffusion bonding of either gold or silver wires. Iakubivskyi et al. [44] proved that silver is not a good choice due to its fast erosion caused by atomic oxygen (conversely, both gold and aluminium resist atomic oxygen). On the other hand, the lack of an oxide layer on gold surface could cause cold welding during the launch phase. Alternatively, Iakubivskyi et al. [44] proposed the "twisted wiring", that is, a manufacturing method in which each bond is achieved by twisting the wires around each other so as to produce a mesh. The strength of this technique is that this type of bond does not pose any limit on the metal alloy that can be used for the tether production, even if its effectiveness has not yet been proven for wires of micrometric thickness and for meshes of centimeter size. However, Iakubivskyi et al. [44] have recently managed to demonstrate the twisting method at a proof-of-concept level for the dimensions of tethers to be used for Coulomb drag propulsion using a manually operated machine. Finally, it should be noted that these last two redundant structures [44] are also capable of withstanding micrometeoroid impacts. Of course, the specific design of the tethers should be done by considering the desired lifetime (i.e., the mission duration) and the expected micrometeoroid flux along the working orbit and the transfer trajectory.

2.4. Materials and thermo-structural analysis

The E-sail performance is significantly affected by the spatial orientation of each single tether, which is the result of complex interactions between the tether stretching induced by the spacecraft spin and its inflection due to the solar wind dynamical pressure. The problem of evaluating the three-dimensional arrangement of the deployed tethers has been addressed by many authors, with different approaches (either numerical or analytical) and model accuracy. This section aims to retrace the evolution of this line of research, which represents a fundamental step for the analysis of an E-sail-based mission.

In 2017, Toivanen and Janhunen [45] modelled the shape of a rotating E-sail with the aim of investigating the problem of spacecraft attitude maintenance and control. In their analysis, the main tethers are assumed to radially extend from the spacecraft hub. The tip of each tether hosts a remote unit and the sail arrangement is completed by auxiliary tethers connecting the remote units at the sail rim; see Fig. 3. Starting from that configuration, Toivanen and Janhunen [45] discussed the numerical solution of an integral equation similar to that of a catenary, which was parameterized by the sail orientation relative to the solar wind direction and the ratio of the electric to the centrifugal force. According to that simplified model, the

(a) Tether bond.

(b) 15 m of tether on the flight reel.

(c) 1 km of tether on the output spool.

Figure 11: Heytethers manufacturing within the framework of the European project EU ESAIL-FP7. Adapted from Ref. [43], courtesy of the authors.

tether assembly describes a cone near the spacecraft main body, while a flat region is present near the tether tips due to the centrifugal force. An analytical approximation of the main tether shape was also proposed, in which the tether displacement outside the sail nominal plane has a quadratic dependence on the distance from the spacecraft spin axis, so that each tether arranges according to a parabolic shape.

The problem of describing the tether equilibrium shape and evaluating the maximum tension force (i.e., the root stress) experienced by the tethers is fairly involved. However, it is greatly simplified when the spacecraft spin axis is aligned with the solar wind velocity vector; see Fig. 12. This is the special case considered by Bassetto et al. [46], who showed that the tether shape and the root stress may be described through closed-form expressions under some simplifying hypotheses. The first one is that, unlike Ref. [45], the tethers do not host tip masses. In the second place the tethers have no bending stiffness, so that only an internal tension acts tangentially to their neutral axis. When the spin rate is sufficiently high, the shape of each tether from root to tip follows a natural logarithmic arc and it is possible to relate the root stress to the spin rate and the tether length.

Recently, the assumptions on which the previous analyses were based have been removed and more complex mathematical tools have been proposed to describe the equilibrium shape and the dynamic behaviour of a large deployed E-sail. More precisely, Liu et al. [47] investigated the attitude dynamics of an E-sail from a multibody perspective by means of a dumbbell model. The latter was then compared to an elastic multipoint model for validation purposes. The results show that the dumbbell model is accurate enough when the spin rate is sufficiently high. Wang et al. [48] proposed an absolute nodal coordinate formulation to define a dynamical model for the tethers subject to both axial and bending deformations. In particular,

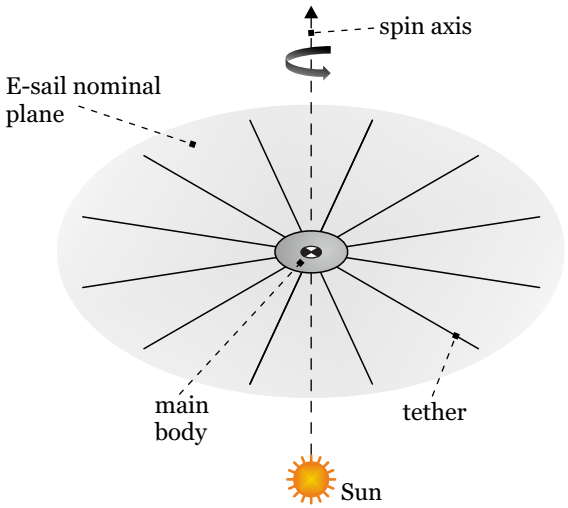

Figure 12: E-sail with a Sun-facing attitude.

they managed to reduce the system degrees of freedom by assembling the tether elements with the shared node method instead of using the constraint equations. The numerical results show that the rotating tethers are affected by large flexible deformations due to the solar wind dynamical pressure.

In this context, Li et al. [49] used a nodal position finite element method to analyze the coupling between the orbital motion and the attitude dynamics of a spinning E-sail (when only the gravitational force is considered) and the interaction between the Coulomb force and the tether elastic motions. In their study [49], the authors assumed the remote units located at the tips to be connected to the main tethers with non-conductive auxiliary tethers and described each tether with a two-node straight truss element so as to guarantee an adequate model accuracy at an acceptable computational cost. The coupling effect between the E-sail dynamical response and the generated thrust is significant for an asymmetrical E-sail, in which variations in both spin rate and tether tension take place. Also, Ref. [49] points out a strong dependence of the thrust vector on the E-sail attitude angles and shows how a high spin rate ensures the E-sail mechanical stability.

An absolute nodal coordinate formulation was also adopted by Zhao et al. [50] for investigating the effects of the solar wind dynamical pressure on an E-sail. Starting from the development of a suitable thrust and an elastic force model and using the kinetic equations, the deformations of the tethers were evaluated under different spin rates and compared to those obtained with a dumbbell model. According to Ref. [50], the oscillation period of the tethers may be shortened by increasing the rotational angular velocity. Moreover, a sufficiently high spin rate allows the structural behaviour of the flexible tethers to be approximated as rigid. In this context, Ren and Yang [51] used a slightly different approach that describes the E-sail dynamic behaviour with a referenced nodal coordinate formulation. This is similar to the absolute nodal coordinate description, but it is formulated in a different reference frame that significantly reduces the computational cost. In particular, the simulation results of Ref. [51] confirm that a high spin rate is required for the structure to obtain a centrifugal force sufficient to resist tether deformations. The corresponding tensions are on the order of 100 times the thrust magnitude acting on the E-sail.

A different approach for modelling the E-sail shape was proposed by Boni et al. [52], who adopted a Finite Element approach to evaluate the deformation of the tethers of a spinning and Sun-facing E-sail; see Fig 13. The analysis aims to provide an estimation of the static deformation of the E-sail, thus neglecting the tether dynamics, using three different beam models to study the tether shape. The Euler-Bernoulli beam element (with cubic shape functions) was chosen for its efficiency in handling the strong non-linearity associated with the bending effect on very slender beams. The convergence difficulties manifested by the Euler-Bernoulli beam element (which neglects the beam shear flexibility) were overcome by the shear-flexible (largely extensible) beam element in its quadratic formulation. In particular, the shear-flexible beam elements are able to model the non-linear stress stiffening, which occurs when the variation of the shear strain

along the beam axis yields a constraint to bending rotations. Boni et al. [52] also tested a hybrid beam element, which optimally matches the properties of the Euler-Bernoulli and shear-flexible beam elements in order to characterize the structural behaviour of highly slender beams subject to multi-axial loads.

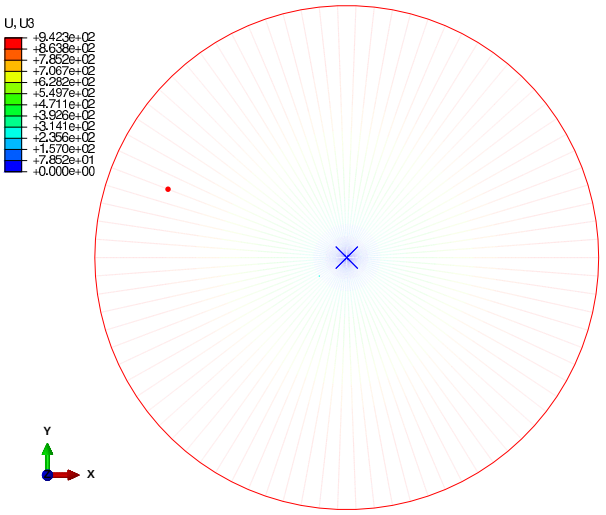

(a) In plane view.

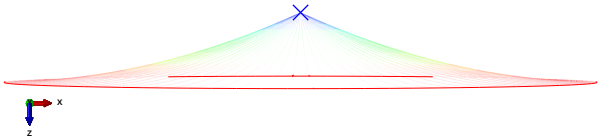

(b) Side view.

Figure 13: Finite element analysis of a Sun-facing E-sail configuration. Adapted from Ref. [52].

It is worth of mentioning the recent work by Lillian [53], who presented an analytical model for the linear vibrations of hub and spoke E-sails in order to facilitate the development of necessary control schemes. The resultant natural frequencies and mode shapes provide insight into the dynamics and stability of an E-sail and lay the foundation for development of control schemes. In addition, Lillian [53] provided a number of simple calculations that accurately estimate many of the natural frequencies and, therefore, could be used to facilitate the design of future E-sails.

We finally quote the thermal stress analysis discussed by Janhunen and Toivanen [54], who investigated the conditions under which the stress induced by eclipses are safe for an E-sail equipped with tethers of 20 km. In fact, when an E-sail is shadowed by a celestial body, the temperature of the tethers suddenly falls down due to their low heat capacity. In turn, such a rapid thermal contraction, combined with the inertia of the remote units located at the tether tips, increases the tensile stress, which may cause a tether failure. The main outcome of this study [54] is that eclipses are safe beyond 2.5 au from the Sun. Instead, eclipsed orbits with high hyperbolic excess speeds are unsafe when the E-sail-based spacecraft flies in the inner Solar System. For this reason, gravity assist maneuvers with Venus, Earth, or Mars may be considered in the mission design only if no eclipse takes place.

3. E-sail thrust and torque vectors

This section illustrates the evolution of the mathematical models that have been formulated to describe the thrust and torque vectors of an E-sail and to study its orbital and attitude dynamics in a heliocentric framework.

3.1. Propulsive acceleration vector models

The E-sail concept was conceived by Janhunen in 2004 [19], who proposed to generate thrust outside the Earth's magnetosphere by using a grid of thin conductive wires immersed in the solar wind; see Fig. 1. According to Ref. [19], if the wires are kept at an electrical voltage of 6 kV with respect to the solar wind plasma and if the distance among the various wires is of the same order as the Debye length λ_{De} of the solar wind plasma, the incoming charged particles sense the E-sail as a barrier and collide with it in such a way as to transfer momentum to the spacecraft. In 2007, Janhunen and Sandroos [55] carried out the first electrostatic plasma simulations and found a first correlation between the Sun-sail distance r and the thrust vector $\boldsymbol{F}$ along the radial direction. They showed that the thrust magnitude $F \triangleq \|\boldsymbol{F}\|$ is proportional to the product between the electron density n_e and the Debye length of the solar wind plasma [55]. In turn, λ_{De} is proportional to the square root of the ratio of the electron temperature T_e to n_e. Since n_e scales as r^{-2} and T_e is proportional to $r^{-1/3}$, it turns out that $F \propto r^{-7/6}$. Moreover, the authors [55] found out that, under average solar wind conditions and at the reference distance $r_\oplus \triangleq 1$ au, the thrust per unit length is about $5 \pm 1 \times 10^{-8}$ N/m when the tether electric potential is 15 kV. Therefore, according to the first version of the E-sail thrust model proposed by Janhunen and Sandroos [55], the propulsive acceleration vector $\boldsymbol{a}$ may be written as

$$\boldsymbol{a} = a_c \left(\frac{r_\oplus}{r}\right)^{7/6} \hat{\boldsymbol{r}} \tag{1}$$

where $\hat{\boldsymbol{r}}$ is the Sun-sail unit vector and a_c is the so-called "characteristic acceleration", that is, the maximum value of $\|\boldsymbol{a}\|$ at the Sun-spacecraft reference distance $r = r_\oplus$.

Starting from the model discussed in Ref. [55], Mengali et al. [56] proposed an extension of Eq. (1) in order to investigate minimum-time transfers between two different Keplerian orbits. In fact, a necessary condition for modifying the angular momentum of the spacecraft osculating orbit is in the possibility of generating a propulsive acceleration component perpendicular to the local radial direction $\hat{\boldsymbol{r}}$. This is achievable by inclining the E-sail nominal plane, that is, the plane containing the wires, which are stretched out by the E-sail spin; see Fig 12. In that case, the E-sail propulsive acceleration vector $\boldsymbol{a}$ may be written as [56]

$$\boldsymbol{a} = a_c \, \tau \left(\frac{r_\oplus}{r}\right)^{7/6} \hat{\boldsymbol{a}} \quad \text{with} \quad \arccos\left(\hat{\boldsymbol{a}} \cdot \hat{\boldsymbol{r}}\right) \triangleq \alpha \in [0, \, \alpha_{\max}] \tag{2}$$

where $\hat{\boldsymbol{a}} \triangleq \boldsymbol{a} / \|\boldsymbol{a}\|$, $\alpha_{\max} < 90$ deg, and $\tau = \{0, \, 1\}$ is a dimensionless switching parameter that is introduced to model the on/off modes of the electron gun; see Fig. 14. In particular, when $\tau = 0$ the E-sail does not

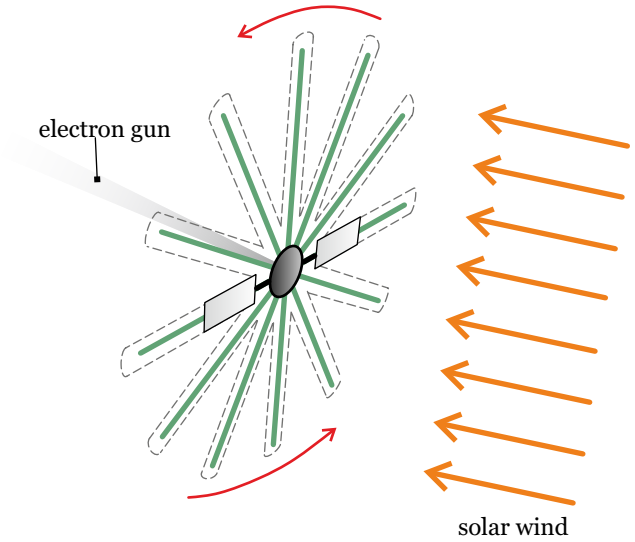

Figure 14: E-sail electron gun scheme.

generate any thrust and the spacecraft covers a Keplerian (or coasting) arc. The angle α between $\hat{\boldsymbol{a}}$ and $\hat{\boldsymbol{r}}$

is the thrust cone angle and is approximately equal to one-half the sail pitch angle α_n. In particular, α_n is defined as the angle between the directions of $\hat{\boldsymbol{r}}$ and $\hat{\boldsymbol{n}}$, the latter being a unit vector normal to the sail nominal plane in the direction opposite to the Sun (i.e., $\hat{\boldsymbol{r}} \cdot \hat{\boldsymbol{n}} > 0$); see Fig. 15. Finally, a constraint on the maximum thrust angle $\alpha_{\max}$, on the order of 30–35 deg (i.e., $\alpha_n \in [0,\, 60\text{–}70]$ deg) is necessary to prevent the E-sail from possible mechanical instabilities. In other words, according to the thrust model discussed in Ref. [56], the E-sail propulsive acceleration vector $\boldsymbol{a}$ is constrained to lie within a conical region as described in Fig. 15, while the value of $\|\boldsymbol{a}\|$ does not depend on the thrust angle α.

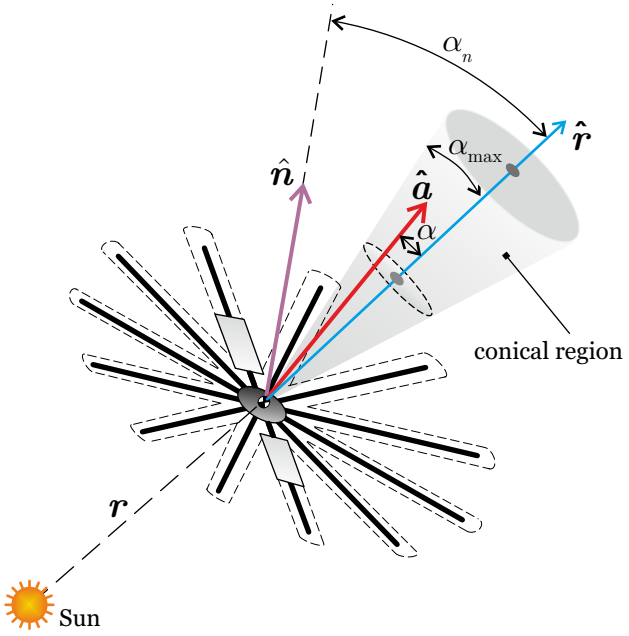

Figure 15: E-sail thrust vector constraint described in Ref. [56].

It is worth noting that Ref. [56] also provides the first and rather involved expression for estimating the characteristic acceleration $a_{c_\oplus}$ at one astronomical unit from the Sun as a function of the solar wind plasma properties and the E-sail design characteristics, viz.

$$a_{c_\oplus} = \frac{6.18\,(1-\eta)\,m_p\,v_{\rm sw}^2\,\sqrt{\dfrac{n_\oplus\,\epsilon_0\,T_{e_\oplus}}{k_B}}}{e_e\,K_t\left(2\,\kappa\,n_\oplus\,r_w\sqrt{\dfrac{2\,e_e^3\,V^3}{m_e}}+\pi\,\rho_w\,r_w^2\right)\sqrt{\exp\left[\dfrac{m_p\,v_{\rm sw}^2}{e_e\,V}\,\ln\left(\dfrac{2}{r_w}\sqrt{\dfrac{\epsilon_0\,T_e}{k_B\,n_\oplus\,e_e^2}}\right)\right]-1}} \tag{3}$$

where η is the payload mass fraction, $m_p \triangleq 1.673\times10^{-31}$ kg is the proton mass, $v_{\rm sw} \simeq 400$ km/s is the speed of solar wind ions, $n_\oplus \simeq 7.3\times10^6$ m^{-3} is the plasma density at $r = r_\oplus$, $\epsilon_0 \triangleq 8.854\times10^{-12}$ C/V is the vacuum permittivity, $T_{e_\oplus} \simeq 1.4\times10^5$ K is the plasma electron temperature at $r = r_\oplus$, $k_B \triangleq 1.38065\times10^{-23}$ J/K is the Boltzmann constant, $e_e \triangleq 1.602\times10^{-19}$ C is the elementary charge, and $m_e \triangleq 9.109\times10^{-31}$ kg is the electron mass. The variables associated with the E-sail design characteristics in Eq. (3) are the tether voltage V, the wire radius r_w, the wire density ρ_w, the mass-to-power ratio κ (on the order of 0.25 kg/W), and K_t is a multiline tether coefficient depending on the tether structure. For example, $K_t \simeq 4.3$ for a Hoytether structure [57], whereas $K_t \simeq 1$ for a Heytether configuration; see Section 2.3 and Figs. 9-10.

The results of subsequent and more refined plasmadynamic simulations described in Ref. [58] led to new important discoveries. The first one is that the thrust per unit of tether length is five times greater than the previously found values, thus affecting the estimation of the characteristic acceleration a_c. The second one concerns the dependence of the thrust magnitude F on the Sun-spacecraft distance r, which predicts an inversely proportional relationship between F and r [59]. In this case, the expression of the E-sail propulsive

acceleration vector becomes [58]

$$\boldsymbol{a} = a_c\,\tau\,\left(\frac{r_\oplus}{r}\right)\hat{\boldsymbol{a}} \tag{4}$$

where, again, $\alpha = \arccos\left(\hat{\boldsymbol{a}}\cdot\hat{\boldsymbol{r}}\right) \simeq \alpha_n/2$ is the thrust angle, with $\alpha_n \in [0,\, 60\text{–}70]\,\text{deg}$.

Further investigations [60] highlighted a more complex relationship between α and α_n and, in addition, reported a variation (i.e., a decrease) in the thrust magnitude F with the sail pitch angle α_n. The new mathematical model is to be attributed to Yamaguchi and Yamakawa [60], who proposed two best-fit interpolations of their numerical data to get the following polynomial relations between α and α_n and between the propulsive acceleration magnitude $\|\boldsymbol{a}\|$ and α_n, viz.

$$\alpha = b_6\,\alpha_n^6 + b_5\,\alpha_n^5 + b_4\,\alpha_n^4 + b_3\,\alpha_n^3 + b_2\,\alpha_n^2 + b_1\,\alpha_n + b_0 \tag{5}$$

$$\gamma \triangleq \frac{\|\boldsymbol{a}\|}{a_c\,\tau\,(r_\oplus/r)} = c_6\,\alpha_n^6 + c_5\,\alpha_n^5 + c_4\,\alpha_n^4 + c_3\,\alpha_n^3 + c_2\,\alpha_n^2 + c_1\,\alpha_n + c_0 \tag{6}$$

where α_n and α are reported in degrees, while the values of coefficients b_i and c_i (with $i = \{0,\,\ldots,\,6\}$) are summarized in Tab. 1.

Table 1: Best-fit coefficients of the polynomial relations by Yamaguchi and Yamakawa [60]; see Eqs. (5)-(6).

i	0	1	2	3	6	5	6
b_i	0	4.853×10^{-1}	3.652×10^{-3}	-2.661×10^{-4}	6.322×10^{-6}	-8.295×10^{-8}	3.681×10^{-10}
c_i	1	6.904×10^{-5}	-1.271×10^{-4}	7.027×10^{-7}	-1.261×10^{-8}	1.943×10^{-10}	-5.896×10^{-13}

The variation of α and γ with α_n is shown in Fig. 16 with red lines. In particular, the linear relationship $\alpha \simeq \alpha_n/2$ is in agreement with Eq. (5) when α_n is less than about 15 deg. When $\alpha_n > 15\,\text{deg}$, instead, the function $\alpha = \alpha(\alpha_n)$ is strongly nonlinear and has a maximum (slightly less than 20 deg) when $\alpha_n \simeq 55\,\text{deg}$, after which it decreases up to zero when $\alpha_n = 90\,\text{deg}$. On the other hand, the dimensionless propulsive acceleration γ always decreases with α_n. In particular, $\gamma \simeq \{1,\, 0.7,\, 0.5\}$ when $\alpha_n = \{0,\, 55,\, 90\}\,\text{deg}$, respectively. Starting from the results of Ref. [60], Quarta and Mengali [62] have proposed an analytical approximation of

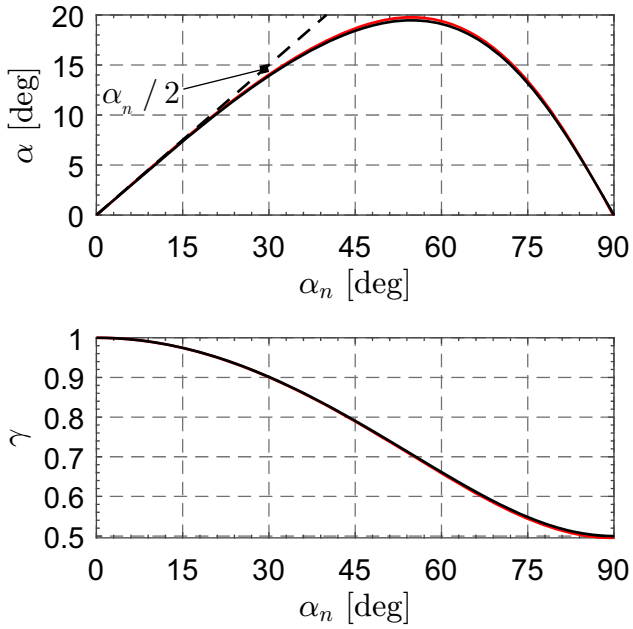

Figure 16: Variation of α and γ with α_n according to Ref. [60] (red lines) and Ref. [61] (black lines).

Eqs. (5)-(6) with the aim of investigating minimum-time trajectories using an indirect approach. According to Ref. [62], the functions $\alpha = \alpha(\alpha_n)$ and $\gamma = \gamma(\alpha_n)$ may be accurately approximated as

$$\alpha \simeq \arctan\left(\frac{R\,\sin(2\,\alpha_n)}{d + R\,\cos(2\,\alpha_n)}\right) \quad , \quad \gamma \simeq \sqrt{d^2 + R^2 + 2\,R\,d\,\cos(2\,\alpha_n)} \tag{7}$$

where $d \simeq 0.7477$ and $R \simeq 0.2523$ are two dimensionless coefficients. The geometric interpretation of the coefficients d and R is given by Fig. 17, which shows, in a dimensionless form, the radial component of the propulsive acceleration $a_r \triangleq \boldsymbol{a} \cdot \hat{\boldsymbol{r}}$ as a function of the transverse component $a_t \triangleq \boldsymbol{a} \cdot \hat{\boldsymbol{t}}$, where $\hat{\boldsymbol{t}}$ is the transverse unit vector ($\hat{\boldsymbol{t}} \cdot \hat{\boldsymbol{r}} = 0$).

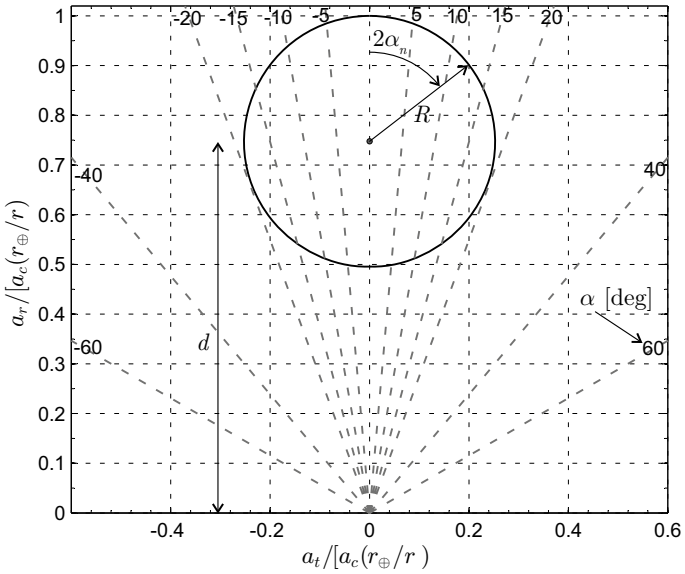

Figure 17: E-sail dimensionless propulsive acceleration components with the thrust model described in Ref. [62].

The most recent and refined mathematical model available to describe the thrust vector provided by a flat E-sail is due to Huo et al. [61], who found a compact description of the propulsive acceleration vector by taking into account the contribution given by any single tether. According to this model [61], the vector $\boldsymbol{a}$ can be analytically written as

$$\boldsymbol{a} = \frac{a_c\,\tau}{2}\left(\frac{r_\oplus}{r}\right)\left[\hat{\boldsymbol{r}} + (\hat{\boldsymbol{r}} \cdot \hat{\boldsymbol{n}})\,\hat{\boldsymbol{n}}\right] \tag{8}$$

where, now, the dependence on α_n is made implicit through the use of $\hat{\boldsymbol{n}}$. In this case, the exact expressions of α and γ are

$$\alpha = \arctan\left(\frac{\sin\alpha_n\,\cos\alpha_n}{1 + \cos^2\alpha_n}\right) \quad , \quad \gamma = \frac{\sqrt{1 + 3\,\cos^2\alpha_n}}{2} \tag{9}$$

which coincide with Eqs. (7) when $d = 3/4$ and $R = 1/4$. The dependence of α and γ on α_n is shown in Fig. 16 with black lines, from which the strong agreement between the models described in Refs. [60] and [61] is evident. Using the analytical description of Eq. (8), the maximum value of α is reached when $\alpha_n = \arccos\left(\sqrt{3}/3\right)$ rad $\simeq 54.74$ deg and its value is $\alpha_{\max} = \arctan\left(\sqrt{2}/4\right) \simeq 19.47$ deg. Finally, the absolute value of the transverse component of the propulsive acceleration is maximum when $\alpha_n = \pi/4$ rad $\equiv 45$ deg. In that case, $\gamma = \sqrt{5/8} \simeq 0.7906$ and $\alpha = \arctan\left(\sqrt{3}/3\right)$ rad $\simeq 18.43$ deg.

The previously discussed mathematical models are valid for a perfectly flat E-sail when all its tethers belong to the sail nominal plane. Toivanen and Janhunen [45] relaxed this assumption to get a parametrization of the E-sail tether shape, as previously discussed. Based on this refined approach, they also derived two expressions for the radial and transverse component of the E-sail propulsive acceleration. The authors [45] pointed out that an increase in the predicted transverse component may be observed with respect to the flat sail case of Eq. (8) due to the fact that a small portion of the E-sail tethers near the tip is parallel to the

spin plane. On the other hand, no significant modification of the thrust angle was observed with respect to the flat E-sail case.

Later, a similar analysis was performed by Bassetto et al. [46], who dealt with the problem of determining an analytical expression of the thrust and torque vectors of an axially-symmetric E-sail with an assigned three-dimensional shape. To obtain their results, the authors [46] made the assumptions that the tethers have a uniform electrical voltage and belong to a plane containing the spacecraft spin axis, around which the tethers are evenly distributed (note that these two hypotheses are not enforced in Ref. [45]). As a result, all the tethers have the same two-dimensional shape, which may be described through a suitable differentiable function $f = f(x)$, where the x-axis is orthogonal to $\hat{\boldsymbol{n}}$ and the generic tether lies on the plane defined by the x-axis and $\hat{\boldsymbol{n}}$. Using the mathematical model discussed in Ref. [46], the propulsive acceleration vector may be expressed as

$$\boldsymbol{a} = \frac{a_c\,\tau}{2}\,\left(\frac{r_\oplus}{r}\right)\,[(2-\mathcal{P})\,\hat{\boldsymbol{r}} + (3\,\mathcal{P}-2)\,\,(\hat{\boldsymbol{r}}\cdot\hat{\boldsymbol{n}})\,\,\hat{\boldsymbol{n}}] \tag{10}$$

where $\mathcal{P} \in [0,\,1]$ is a dimensionless coefficient related to the tether shape s through the equation

$$\mathcal{P} \triangleq \frac{1}{\mathcal{L}}\int_0^{x_t} \frac{\mathrm{d}x}{\sqrt{1+(s')^2}} \tag{11}$$

x_t is the distance of the tether tip from the sail spin axis, and $\mathcal{L}$ the generic tether length defined as

$$\mathcal{L} \triangleq \int_0^{x_t} \sqrt{1+(s')^2}\,\mathrm{d}x \tag{12}$$

In this case, α and γ are given by

$$\alpha = \arctan\left(\frac{\sin\alpha_n\,\cos\alpha_n}{\dfrac{2-\mathcal{P}}{3\,\mathcal{P}-2}+\cos^2\alpha_n}\right) \quad , \quad \gamma = \sqrt{(1-\mathcal{P})\,\sin^2\alpha_n + \frac{\mathcal{P}^2\,\left(1+3\,\cos^2\alpha_n\right)}{4}} \tag{13}$$

In the special case of a flat E-sail (when $s = s' = 0$), Eqs. (11)-(12) give $\mathcal{P} = 1$ and $\mathcal{L} = x_t$ and, as such, Eqs. (10)-(13) reduce to Eqs. (8) and (9), respectively.

Recently, Yamaguchi and Miyata [63] formulated an advanced solar wind force model by numerically determining the shape of the conductive tethers due to the combined effects of centrifugal force and solar wind dynamical pressure. Consistently with the analytical results by Bassetto et al. [46], the authors [63] found that the angle between the thrust vector and the local radial direction ranges between 13 deg and 19 deg. Moreover, the authors [63] proposed best-fit polynomial equations to describe the E-sail thrust vector, which is the resultant of the solar wind force vectors exerted on each tether.

Finally, Du et al. [64] have recently provided the expression of the thrust vector in the form of polynomial expressions from the interpolation of simulation results, the latter obtained by considering the coning motion of the tethers. A comparison of those polynomial expressions with previous results (obtained without including the coning motion) reveals that the coning motion has negligible effects on the E-sail dynamics.

3.2. Torque vector models

Using the parameterized shape of the tethers discussed in Section 2.4, Toivanen and Janhunen [45] found an expression for the torque generated by an elementary tether length, which may be numerically integrated to obtain the total torque generated by the E-sail. They showed that a torque-free condition is achievable with a suitable voltage modulation of each single tether.

A compact expression of the propulsive torque vector $\boldsymbol{T}$ is given in Ref. [46], assuming that all tethers lie on a plane containing the spin axis and a constant voltage acts along each tether. An axially-symmetric E-sail with a uniform electrical voltage generates a torque vector $\boldsymbol{T}$ described by the equation

$$\boldsymbol{T} = \frac{a_c\,m\,L\,\mathcal{M}\,\tau}{2}\,\left(\frac{r_\oplus}{r}\right)\,(\hat{\boldsymbol{n}}\times\hat{\boldsymbol{r}}) \tag{14}$$

where m is the total spacecraft mass and $\mathcal{M} \in [0,\,1]$ is a dimensionless coefficient related to the generic

tether shape s through the equation

$$\mathcal{M} \triangleq \frac{1}{\mathcal{L}^2} \int_0^{x_t} \frac{s\,\left[1+2\,(s')^2\right]+x\,s'}{\sqrt{1+(s')^2}}\,\mathrm{d}x \tag{15}$$

The special case of perfectly stretched tethers yields $\mathcal{M}=0$, that is, a flat E-sail with a uniform electrical voltage does not generate any torque.

4. E-sail heliocentric dynamics

This section summarizes a possible set of differential equations that may be used for describing the heliocentric motion of a spacecraft under the action of the propulsive force and torque provided by a rigid and axially-symmetric E-sail with a uniform electrical voltage. In the literature, the motion and the attitude dynamics are often studied separately due to the marked separation between the two characteristic timescales [65]. In fact, the orbital mean motion (about $1.99\times10^{-7}\,\mathrm{rad/s}$ for a heliocentric circular orbit of radius equal to 1 au) is usually several orders of magnitude smaller than the typical angular velocity of the spacecraft about its center of gravity.

4.1. Orbital dynamics

Consider an E-sail that is traveling a heliocentric parking orbit of given characteristics. The spacecraft is modelled as a point mass S subject to the gravitational force of the Sun and to the E-sail thrust. To make the equations of orbital dynamics free from singularities, the spacecraft state is often defined by a set of non-singular Modified Equinoctial Orbital Elements [66, 67] (MEOEs) $\{p,\,f,\,g,\,h,\,k,\,L\}$, which are related to the classical orbital elements $\{a,\,e,\,i,\,\Omega,\,\omega,\,\nu\}$ of the osculating orbit by the following relationships

$$p=a\,\left(1-e^2\right)\quad,\quad f=e\,\cos(\Omega+\omega)\quad,\quad g=e\,\sin(\Omega+\omega)\quad,$$

$$h=\tan\left(i/2\right)\,\cos\Omega\quad,\quad k=\tan\left(i/2\right)\,\sin\Omega\quad,\quad L=\nu+\Omega+\omega \tag{16}$$

where a is the semimajor axis, e is the orbital eccentricity, i is the orbital inclination, Ω is the right ascension of the ascending node, ω is the argument of perihelion, and ν is the true anomaly. The heliocentric motion of the E-sail is described by the vectorial differential equation [68]

$$\dot{\boldsymbol{x}} = \mathbb{A}\,\left[\boldsymbol{a}\right]_{\mathcal{T}_{\mathrm{RTN}}} + \boldsymbol{c} \tag{17}$$

where $\boldsymbol{x}\triangleq[p,\,f,\,g,\,h,\,k,\,L]^{\mathrm{T}}$ is the state vector, $\mathbb{A}\in\mathbb{R}^{6\times3}$ is the state matrix, defined as

$$\mathbb{A}\triangleq\sqrt{\frac{p}{\mu_\odot}}\begin{bmatrix} 0 & \dfrac{2\,p}{q} & 0 \\ \sin L & \dfrac{(q+1)\,\cos L+f}{q} & \dfrac{g\,(k\,\cos L-h\,\sin L)}{q} \\ -\cos L & \dfrac{(q+1)\,\sin L+g}{q} & \dfrac{f\,(h\,\sin L-k\,\cos L)}{q} \\ 0 & 0 & \dfrac{(1+h^2+k^2)\,\cos L}{2\,q} \\ 0 & 0 & \dfrac{(1+h^2+k^2)\,\sin L}{2\,q} \\ 0 & 0 & \dfrac{h\,\sin L-k\,\cos L}{q} \end{bmatrix} \tag{18}$$

and

$$\boldsymbol{c}\triangleq\sqrt{\mu_\odot\,q^4/p^3}\,[0\quad 0\quad 0\quad 0\quad 0\quad 1]^{\mathrm{T}} \tag{19}$$

where $q\triangleq 1+f,\cos L+g\,\sin L>0$ is the ratio of the semilatus rectum p to the orbital radius r and $\mu_\odot\simeq1.327\times10^{11}\,\mathrm{km}^3/\mathrm{s}^2$ is the Sun's gravitational parameter. According to Eq. (17), the components of $\boldsymbol{a}$

must be written in the radial-transverse-normal reference frame $\mathcal{T}_{\rm RTN}$ of unit vectors

$$\hat{\boldsymbol{e}}_r \triangleq \hat{\boldsymbol{r}} \quad , \quad \hat{\boldsymbol{e}}_n \triangleq \frac{\hat{\boldsymbol{e}}_r \times \boldsymbol{v}}{||\hat{\boldsymbol{e}}_r \times \boldsymbol{v}||} \quad , \quad \hat{\boldsymbol{e}}_t \triangleq \hat{\boldsymbol{e}}_n \times \hat{\boldsymbol{e}}_r \tag{20}$$

where $\boldsymbol{v}$ represents the spacecraft inertial velocity; see Fig. 18. Using the definitions of α and γ of Section 3.1,

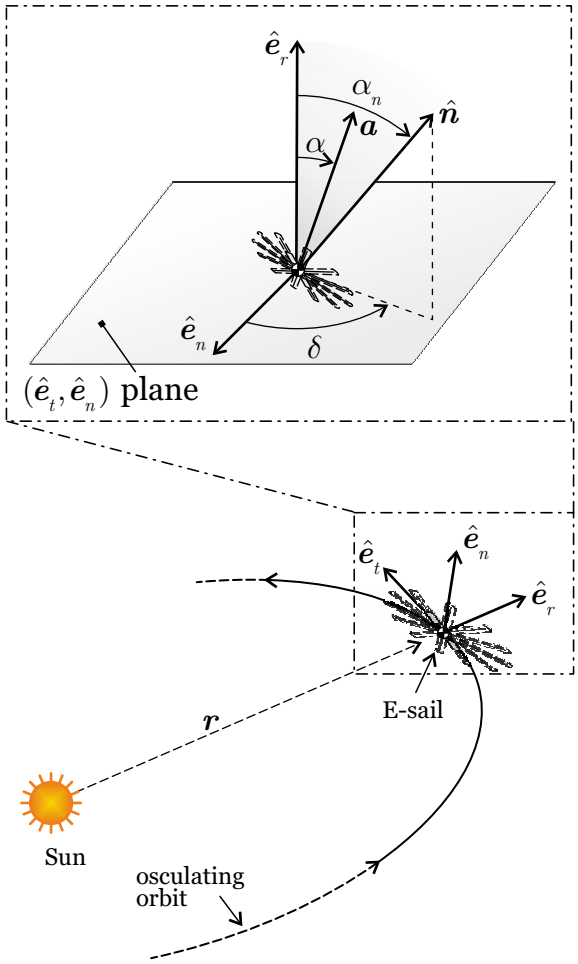

Figure 18: Reference frame and E-sail characteristic angles.

the components of $\boldsymbol{a}$ in $\mathcal{T}_{\rm RTN}$ are

$$[\boldsymbol{a}]_{\mathcal{T}_{\rm RTN}} \triangleq [a_r \quad a_t \quad a_n]^{\rm T} = a_c\, \tau\, \gamma \left(\frac{r_\oplus}{r}\right) [\cos\alpha \quad -\sin\alpha\, \sin\delta \quad \sin\alpha\, \cos\delta]^{\rm T} \tag{21}$$

where the clock angle $\delta \in [0,\, 2\pi)$ rad is measured counterclockwise from $\hat{\boldsymbol{e}}_n$ to the projection of $\hat{\boldsymbol{n}}$ on the local horizontal plane (i.e., the plane $(\hat{\boldsymbol{e}}_t,\, \hat{\boldsymbol{e}}_n)$ perpendicular to the Sun-spacecraft line); see Fig. 18. According

to the model proposed by Huo et al. [61], the components of $\boldsymbol{a}$ in $\mathcal{T}_{\mathrm{RTN}}$ are

$$a_r = \frac{a_c\,\tau}{2}\left(\frac{r_\oplus}{r}\right)\left(1+\cos^2\alpha_n\right) \tag{22}$$

$$a_t = -\frac{a_c\,\tau}{2}\left(\frac{r_\oplus}{r}\right)\cos\alpha_n\,\sin\alpha_n\,\sin\delta \tag{23}$$

$$a_n = \frac{a_c\,\tau}{2}\left(\frac{r_\oplus}{r}\right)\cos\alpha_n\,\sin\alpha_n\,\cos\delta \tag{24}$$

where the Sun-spacecraft distance may be expressed in terms of MEOEs as $r = p/q$.

Another approach used for calculating the E-sail trajectory was proposed by Niccolai et al. [69], who applied a perturbative approach and an asymptotic series expansion to the problem of E-sail trajectory determination with fixed pitch angle [70, 71, 72]. The authors obtained analytical approximations of the variation of a set of modified nonsingular parameters as a function of an angular coordinate and showed that a remarkable model accuracy is possible with the aid of suitable orbital rectifications.

4.2. Attitude dynamics

To a first approximation, the attitude dynamics of an E-sail may be studied under the simplifying assumption that it behaves like a rigid body [65]. A natural choice is therefore to describe the attitude motion through the Euler's equations, which are written with the aid of the three usual Euler's angles $\{\phi,\,\theta,\,\psi\}$ that define the orientation of a body-fixed reference frame $\mathcal{T}_B\left(S;\hat{\boldsymbol{\imath}}_B,\hat{\boldsymbol{\jmath}}_B,\hat{\boldsymbol{k}}_B\right)$, with origin at the spacecraft center of mass, with respect to an inertial frame $\mathcal{T}_I\left(S;\hat{\boldsymbol{\imath}}_I,\hat{\boldsymbol{\jmath}}_I,\hat{\boldsymbol{k}}_I\right)$ with the same origin. Without loss of generality, assume that $\hat{\boldsymbol{k}}_B \equiv \hat{\boldsymbol{n}}$ and $\hat{\boldsymbol{k}}_I \equiv \hat{\boldsymbol{r}}$ and adopt a rotational sequence $3(\psi) \rightarrow 1(\phi) \rightarrow 2(\theta)$ [73] to describe the orientation of $\mathcal{T}_B$ relative to $\mathcal{T}_I$. Accordingly, the kinematic equations of a rigid E-sail are [65]

$$\dot{\phi} = \Omega_x\,\cos\theta + \Omega_z\,\sin\theta \tag{25}$$

$$\dot{\theta} = \Omega_y - \left(\Omega_z\,\cos\theta - \Omega_x\,\sin\theta\right)\tan\phi \tag{26}$$

$$\dot{\psi} = \left(\Omega_z\,\cos\theta - \Omega_x\,\sin\theta\right)\sec\phi \tag{27}$$

where $\{\Omega_x,\,\Omega_y,\,\Omega_z\}$ are the components of the spacecraft angular velocity $\boldsymbol{\Omega}$ in $\mathcal{T}_B$. The Euler's equations may be written by first determining the components of $\hat{\boldsymbol{r}}$ and $\hat{\boldsymbol{n}}$ in $\mathcal{T}_B$, which are, by construction

$$[\hat{\boldsymbol{n}}]_{\mathcal{T}_B} = [0 \quad 0 \quad 1]^{\mathrm{T}} \quad , \quad [\hat{\boldsymbol{r}}]_{\mathcal{T}_B} = [-\cos\phi\,\sin\theta \quad \sin\phi \quad \cos\phi\,\cos\theta]^{\mathrm{T}} \tag{28}$$

For example, using the torque vector model conceived by Bassetto et al. [46], the components of the $\boldsymbol{T}$ in $\mathcal{T}_B$ are

$$[\boldsymbol{T}]_{\mathcal{T}_B} = -\frac{a_c\,m\,L\,\mathcal{M}\,\tau}{2}\left(\frac{r_\oplus}{r}\right)[\sin\phi \quad \cos\phi\,\sin\theta \quad 0]^{\mathrm{T}} \tag{29}$$

The resulting Euler's equations are

$$\dot{\Omega}_x = \frac{I_t - I_z}{I_t}\,\Omega_y\,\Omega_z - \frac{a_c\,m\,L\,\mathcal{M}\,\tau}{2\,I_t}\left(\frac{r_\oplus}{r}\right)\sin\phi \tag{30}$$

$$\dot{\Omega}_y = \frac{I_z - I_t}{I_t}\,\Omega_x\,\Omega_z - \frac{a_c\,m\,L\,\mathcal{M}\,\tau}{2\,I_t}\left(\frac{r_\oplus}{r}\right)\cos\phi\,\sin\theta \tag{31}$$

$$\dot{\Omega}_z = 0 \tag{32}$$

where I_t and I_z are the spacecraft longitudinal and transverse moments of inertia, respectively.

5. E-sail control strategies

The mathematical tools discussed in the previous section may be used to find the optimal steering law necessary for an E-sail to reach a target state. To do so, the E-sail must be capable of performing attitude maneuvers, which are also required for maintaining the working orbit in many potential mission scenarios. This section discusses the strategies used for E-sail orbital and attitude control.

5.1. Orbital control

The orbital motion control depends on the calculation of the time evolution of $\{\alpha_n(t), \delta(t), \tau(t)\}$; see Eq. (21). Typically, the control law necessary for an E-sail to bring the spacecraft from a given initial condition to a final one is found by minimizing an assigned cost function.

Since E-sails are propellantless propulsion systems, the cost function is the total flight time for a given characteristic acceleration or, equivalently, the characteristic acceleration for a given total flight time. Minimum-time heliocentric transfers have been extensively investigated in Refs. [62, 74, 75, 76, 77, 78] using indirect methods for trajectory optimization. According to the Pontryagin's maximum principle, the optimal control law maximizes, at any time, the Hamiltonian function of the system. With reference to Eq. (17) the Hamiltonian function is

$$\mathcal{H} \triangleq \left(\mathbb{A}\ [\boldsymbol{a}]_{\mathcal{T}_{\mathrm{RTN}}} + \boldsymbol{c}\right) \cdot \boldsymbol{\lambda} \tag{33}$$

where $\boldsymbol{\lambda} \triangleq [\lambda_p \quad \lambda_f \quad \lambda_g \quad \lambda_h \quad \lambda_k \quad \lambda_L]^{\mathrm{T}}$ is the adjoint (or costate) vector. The time derivative of $\boldsymbol{\lambda}$ is given by the Euler-Lagrange equation, viz.

$$\dot{\boldsymbol{\lambda}} = -\frac{\partial \mathcal{H}}{\partial \boldsymbol{x}} \tag{34}$$

As a result, the two-point boundary value problem is constituted by 12 scalar equations (6 equations of motion and 6 Euler-Lagrange equations) and the corresponding 12 boundary conditions are related to the desired states at the initial (t_0) and final (t_f) times. The transversality condition $\mathcal{H}(t_f) = 1$ is used to obtain the minimum transfer time. The maximization of $\mathcal{H}$ amounts to maximizing the projection of $\boldsymbol{a}$ along the Lawden's primer vector [79].

Several other approaches have been proposed in the literature for finding the minimum time trajectory of an E-sail, most of which are based on direct optimization methods. Their main advantage is that they avoid the need to solve the two-point boundary value problem, which is very sensitive to the initial guess of the costate variables. For example, Wang et al. [80] used the particle swarm optimization algorithm to find minimum-time transfers from Earth to Mars and Venus. The particle swarm optimization was first used to obtain a nearly optimal trajectory after a suitable discretization of the control variables that transform the optimal control problem into a parameter optimization problem of nonlinear programming. The particle swarm optimization was then exploited again to optimize the parameters of a designed control law that approximates the previously obtained optimal trajectory. The simulation results show that the random selection of initial variables ensures large convergence range and robustness. The problem of optimizing an E-sail trajectory for outer Solar System exploration was addressed by Qi et al. [81] by means of Gauss pseudospectral methods. Assuming that the E-sail characteristic acceleration varies as a consequence of solar storms, the authors included the solar wind uncertainties in the model, thus improving its adaptability. Huo et al. [82] presented a hybrid optimization method, which combines a genetic algorithm and Gauss pseudospectral methods, for evaluating the minimum-time Earth-Mars and Earth-Venus transfer trajectories. The proposed formulation effectively combines the global search ability of the genetic algorithm and the high convergence rate of sequential quadratic programming. In fact, the authors [82] interpolates the initial guesses of states and controls in the Gauss pseudospectral methods using the best solution obtained from a genetic algorithm. The numerical simulations show that such a hybrid optimization method is able to reach the (feasible) global optimal solution of the E-sail trajectory without any initial guess. The same approach was also used by Huo et al. [83] for investigating minimum-time transfer trajectories from Earth to the asteroid Ceres using the thrust model discussed in Ref. [60].

Locally optimal formulations have also been investigated in the literature, which usually require less computational efforts when compared to global optimization strategies, but still provide useful results. For example, Bassetto et al. [84] analyzed near optimal heliocentric transfers by looking for the control laws $\alpha_n(t)$, $\delta(t)$, and $\tau(t)$ that maximize (or minimize) the instantaneous time derivative of one orbital parameter

or a linear combination of them. When the propulsive acceleration vector $\boldsymbol{a}$ is constrained to belong to the osculating orbital plane (i.e., $a_n = 0$) or to the plane $(\hat{\boldsymbol{e}}_r, \hat{\boldsymbol{e}}_n)$ (i.e., $a_t = 0$), then δ can only take two values. In the former case $\delta = \{\pi/2, 3\pi/2\}$ rad, while in the latter one $\delta = \{0, \pi\}$ rad. In these particular cases, δ can be removed from the set of control variables with the assumption that α_n can also take negative values, that is, $\alpha_n \in [-\alpha_{n_{\max}}, \alpha_{n_{\max}}]$, where $\text{sign}(\alpha_n) = \text{sign}(\boldsymbol{a} \cdot \hat{\boldsymbol{e}}_t)$ if $a_n = 0$ and $\text{sign}(\alpha_n) = \text{sign}(\boldsymbol{a} \cdot \hat{\boldsymbol{e}}_n)$ if $a_t = 0$. When the optimization process involves a single orbital element $\text{œ} \in \{a, e, i, \Omega, \omega, \nu\}$ only, the locally optimal value of α_n can be analytically found by enforcing the necessary condition

$$\frac{\partial}{\partial \alpha_n}\left(\frac{\mathrm{d}\text{œ}}{\mathrm{d}t}\right) = 0 \tag{35}$$

Using the propulsive acceleration model of Eqs. (4)-(7) [62], Ref. [84] provides the values of α_n (namely, α_{n_1} and α_{n_2}) that solve Eq. (35), viz.

$$\alpha_{n_1} = \arcsin\left(\sqrt{\frac{k_{\text{œ}}^2 - k_{\text{œ}}\sqrt{k_{\text{œ}}^2+1}+1}{2\,(k_{\text{œ}}^2+1)}}\right) \quad , \quad \alpha_{n_2} = \alpha_{n_1} - \frac{\pi}{2} \tag{36}$$

where the functions $k_{\text{œ}}$ are given by

$$k_a = \frac{e\,\sin\nu}{1+e\,\cos\nu} \tag{37}$$

$$k_e = \frac{\sin\nu\,(1+e\,\cos\nu)}{e\,\cos^2\nu + 2\,\cos\nu + e} \tag{38}$$

$$k_\omega = -\frac{(1+e\,\cos\nu)\,\cos\nu}{(2+e\,\cos\nu)\,\sin\nu} \tag{39}$$

$$k_i = k_\Omega = 0 \tag{40}$$

The maximum of $\mathrm{d}\text{œ}/\mathrm{d}t$ is $\max\left(\mathrm{d}\text{œ}/\mathrm{d}t|_{\alpha_n=\alpha_{n_1}}, \mathrm{d}\text{œ}/\mathrm{d}t|_{\alpha_n=\alpha_{n_2}}\right)$, whereas the minimum of $\mathrm{d}\text{œ}/\mathrm{d}t$ is $\min\left(\mathrm{d}\text{œ}/\mathrm{d}t|_{\alpha_n=\alpha_{n_1}}, \mathrm{d}\text{œ}/\mathrm{d}t|_{\alpha_n=\alpha_{n_2}}\right)$. The corresponding switching parameter is chosen by looking at the sign of $\max(\mathrm{d}\text{œ}/\mathrm{d}t)$ (or $\min(\mathrm{d}\text{œ}/\mathrm{d}t)$). In particular, if $\max(\mathrm{d}\text{œ}/\mathrm{d}t) < 0$, then $\tau = 0$, while $\tau = 1$ if $\max(\mathrm{d}\text{œ}/\mathrm{d}t) > 0$. On the other hand, if the time derivative of the orbital parameter is to be minimized, a switching parameter $\tau = 0$ must be chosen if $\min(\mathrm{d}\text{œ}/\mathrm{d}t) > 0$, while $\tau = 1$ if $\min(\mathrm{d}\text{œ}/\mathrm{d}t) < 0$.

Another strategy that may be exploited to determine the required control law is to assume that the E-sail has to follow an assigned trajectory, and to find the corresponding required time history of the control variables. Such strategies are called shape-based methods, and have been recently investigated by Bassetto et al. [85], who calculated the purely radial propulsive acceleration that is required for a generalized sail to follow a heliocentric spiral trajectory in the form

$$r = r_0\left(\frac{\varphi}{\varphi_0}\right)^\beta \tag{41}$$

where $\beta \in \mathbb{R}_{\neq 0}$ is a dimensionless parameter that characterizes the type of spiral, while φ is the polar angle, measured anticlockwise from φ_0, defined as

$$\varphi_0 \triangleq \frac{\beta\, v_{\varphi_0}}{v_{r_0}} \tag{42}$$

being v_{φ_0} and v_{r_0} the circumferential and radial velocities, respectively, at the initial time t_0. The solution for $\varphi(t)$ is [85]

$$\varphi(t) = \begin{cases} C_2\,[C_1 + (1+2\,\beta)\,t]^{\frac{1}{1+2\,\beta}} & \text{if} \quad \beta \neq \{-1/2,\, 0\} \\ C_2\,\exp(C_1\,t) & \text{if} \quad \beta = -1/2 \end{cases} \tag{43}$$

where $\{C_1,\, C_2\}$ are two constants of integration, given by

$$C_1 = \begin{cases} \dfrac{\beta\, r_0}{v_{r_0}} & \text{if} \quad \beta \neq \{-1/2,\, 0\} \\ -\dfrac{2\, v_{r_0}}{r_0} & \text{if} \quad \beta = -1/2 \end{cases} \quad , \quad C_2 = \begin{cases} \dfrac{v_{\varphi_0}}{r_0} \left(\dfrac{\beta\, r_0}{v_{r_0}} \right)^{\frac{2\,\beta}{1+2\,\beta}} & \text{if} \quad \beta \neq \{-1/2,\, 0\} \\ -\dfrac{v_{\varphi_0}}{2\, v_{r_0}} & \text{if} \quad \beta = -1/2 \end{cases} \tag{44}$$

When dealing with an E-sail, the characteristic acceleration that is required to follow such spirals is

$$a_c = -\frac{(1+\beta)\, v_{r_0}^2}{\beta\, r_\oplus} \left(\frac{r_0}{r} \right)^{\frac{2+2\,\beta}{\beta}} - \frac{v_{\varphi_0}^2}{r_\oplus} \left(\frac{r_0}{r} \right)^2 + \frac{\mu_\odot}{r_\oplus\, r_0} \left(\frac{r_0}{r} \right) \tag{45}$$

According to Eq. (45), the variation of a_c may be obtained by modulating the switching parameter τ with continuity in the range $[0,\, 1]$. In fact, assuming that $a_{c_{\max}}$ is the maximum required characteristic acceleration during the whole spiral trajectory that the E-sail must travel, the single control parameter is

$$\tau = \frac{a_c}{a_{c_{\max}}} \tag{46}$$

where a_c is given by Eq. (45). The modulation of τ may be achieved by properly adjusting the tether electrical voltage.

Finally, Bassetto et al. [65] dealt with a feedback control system that is able to stabilize the dynamics of a spinning E-sail-based spacecraft around a heliostationary position at a distance of about one astronomical unit from the Sun. The heliostationary condition is known to be unstable [86] and, accordingly, a small error in orbit insertion causes the spacecraft to move away from the prescribed reference position. A suitable modulation of the E-sail electrical voltage allows the spacecraft center of mass to move along the Sun-spacecraft line around its nominal heliostationary position. In particular, with a simple proportional controller, the maximum variation in tether voltage is proportional to the error in orbit insertion and the resulting motion is an undamped harmonic oscillation with a period on the order of some years. The radial oscillations may be damped out by means of a proportional-derivative control system.

5.2. Attitude control

The E-sail attitude control is of primary importance for the correct orientation of the thrust vector during the space mission. In the last decade, several strategies have been proposed both for the maintenance and control of the E-sail attitude and for the regulation of the plane spin rate. This section is devoted to reviewing most of these control strategies, which to date represent only theoretical proposals.

In 2013, Janhunen [31] suggested to apply an auxiliary propulsion to the tips of the main tethers in order to create and modify the E-sail spin rate in such a way as to counteract the orbital Coriolis effect. The results of this work [31] are based on a simple dynamical model of the tether, which is described as a spherical pendulum rotating under the constant action of the solar wind. The tips of the main tethers are assumed to be equipped with small photonic blades, that is, small reflective membranes that collect the solar radiation pressure; see Fig. 5. Janhunen considered this strategy a feasible and attractive solution because it has the benefit of providing sufficient spin control capability while keeping the technology fully propellantless. In the same year, Toivanen and Janhunen [25] proposed to control the E-sail attitude by individually modulating the voltage of each tether in such a way as to produce a net torque on the whole E-sail. In particular, Toivanen and Janhunen [25] calculated the voltage modulation that is required to maintain any realistic sail orientation relative to the Sun-spacecraft line under stationary solar wind conditions. Moreover, the determination of the required modulation provided an estimate of the fraction of the electron gun power to be allocated for attitude control. The authors [25] also showed that orbiting around the Sun with a constant attitude leads to a gradual increase (or decrease) in the sail spin rate when spiraling outward (or inward). This phenomenon arises due to the cumulative effect on the spin rate of the modulation of the E-sail force, which partially cancels the Coriolis effect and partially lays on the spin plane. Finally, Ref. [25] provided the tether spin rate and the coning angle (the angle between the generic tether and the spin plane) as a function of the time variations in solar wind dynamical pressure, tether length, and sail orientation.

In a subsequent work [45], previously mentioned in Section 2.4, Toivanen and Janhunen used an approximate expression of the tether shape to estimate the thrust and torque vectors generated by an E-sail and provided the tether voltage modulation that is required for attitude maintenance in a torque-free solution. They showed [45] that the required amplitude is smaller than that previously found for a single rigid tether resembling a spherical pendulum, thus implying that less thrusting margin is required for attitude maintenance. In this context, Wang et al. [48] applied the same strategy of modulating the tether electrical voltage in order to generate the required control torque. In that case [48], the authors defined equivalent coning and phasing angles for describing the tether deformation, which were successfully used for attitude control design. The use of the equivalent parameters was suitable for controlling an E-sail with long flexible tethers.

More recently, Bassetto et al. [87] showed that the deformation of the tethers due to the combined effects of solar wind dynamical pressure and centrifugal force gives rise to a disturbing torque, which exists even if the tether electrical voltage is uniform and is zero only when the sail spin axis is parallel to the Sun-spacecraft line, that is, in a Sun-facing condition; see Fig. 12. Such a disturbing torque induces a perturbation on the orientation of the thrust vector that tends to be realigned with the Sun-spacecraft line, thus reducing the maneuvering capabilities of the E-sail-based spacecraft. Numerical simulations [65] show that the combined effect of tether inflection and deviation from the Sun-facing condition (that is, the onset of a small pitch angle) generates a nutation motion and a disturbing torque that induces a stable, but undamped, precession with a frequency comparable to the spacecraft spin rate. An effective control law may be used to remove the disturbing torque by slightly adjusting the voltage of each single tether. The proposed solution is also able to maintain the thrust magnitude at its nominal level.

Under the assumption that the E-sail behaves like an axially-symmetric rigid body, Ref. [88] proposed an analytical control law, depending the actual spin plane orientation, which is able to actively control and maintain the spin plane attitude through the individual modulation of the tether electrical voltage. In this case, the simulations show that a small variation of the voltage level is sufficient in most practical circumstances. The proposed method is simple to implement and offers good performance in terms of attitude reorientation times. The numerical simulations of Ref. [88] also reveal that the attitude variation induces the onset of a torque along the E-sail spin axis, which is responsible (together with the disturbance torque due to the tether bending) of a small variation of the sail spin rate. As a result, at the end of the attitude maneuver, the pitch angle is not maintained at a constant value, but tends to slowly decrease with time. Such an unwanted phenomenon is instead absent when the torque along the spin axis is zero or the E-sail shape is perfectly flat. Finally, Bassetto et al. [88] showed that, when the E-sail is made of a few tethers, the control torque necessary for maintaining the final attitude is small compared to the one required for attitude variation. In those cases, the approximation of flat sail becomes accurate enough and useful for greatly simplifying the mission analysis and as a first step towards the study of more refined control laws.

Recently, Li [89] dealt with the coupling effects between the elastic dynamics of the tethers and the electric field with the aim of investigating the flight dynamics and the control strategy of an E-sail model based on the nodal position finite element method. In particular, Li [89] proposed a modified throttling control strategy to command the E-sail attitude by modulating the tether voltage synchronously with the spinning motion. Moreover, the effects of four physical parameters (the number of tethers, the tether length, the sail spin rate, and the mass of remote units) on the orbital and attitude dynamics were investigated, showing that both the maneuverability and the traveled orbital distance increase when the number of main tethers increases, while they decrease when the initial spin rate and the mass of the remote unit increase. In addition, Li [89] observed that, when the length of the main tethers increases, the maneuverability decreases and the traveled orbital distance increases. Finally, Li [89] investigated the effects of the solar wind speed relative to an E-sail and a TI-type E-sail, the latter being a configuration proposed to suppress the spin rate variation during the attitude maneuver thanks to the generation of a thrust component on the sail spin plane [27] (see Section 2.1). The numerical results showed that the relative solar wind speed has a significant effect on the spin rate of the E-sail during an attitude maneuver, while the proposed control strategy is able to successfully stabilize the E-sail spin rate when the TI-type configuration is adopted.

The work by Huang et al. [90] focused on the attitude dynamics and control of another E-sail configuration, that is, a barbell E-sail. Such a concept consists of two tip satellites connected through long conductive tethers to a central insulated confluence point. The electrical insulation between the two tethers allows their electrical voltages to be controlled independently. Huang et al. [90] proposed a nonsingular formulation based on the dumbbell assumption to describe the attitude dynamics of the barbell E-sail under the action

of solar wind dynamical pressure and gravity gradient. The also developed a nonlinear predictive controller (assuming a rigid E-sail) for its attitude adjustment and maintenance through the regulation of the tether voltages [90]. In particular, the efficiency and performance of the nonlinear model predictive control law was tested and demonstrated through a campaign of numerical simulations, which also evaluated the influences of both the initial/final conditions and the controller parameters on the dynamical response of the system [90].

The latest works concerning the E-sail attitude analysis are those by Du et al. [64, 91]. In Ref. [64], the authors investigated the dynamical characteristics of the coning and attitude motion of an E-sail by considering high-order modes of flexible elastic wires. The elastic tethers are described with the nodal position finite element method and discretized into inter-connected two-nodes tensile elements. The central spacecraft and the remote units, instead, are modelled as simple lumped masses. The assumption is made that the spacecraft is flying around the Sun on the ecliptic plane at a distance of one astronomical unit from the primary. The authors investigated how the thrust vector models and the initial E-sail attitude affect the dynamical characteristics of the coning and attitude motion of the sail nominal plane. Under the hypothesis of small coning angles, Du et al. [64] provided an analytical expression of the coning motion frequency, while a parametric analysis revealed that the thrust magnitude does not significantly affect neither the sail and thrust angles nor the E-sail spin rate. Finally, Du et al. [91] dealt with the modelling of rigid-flexible coupling effects on the attitude dynamics and the spin control of an E-sail. In that paper, the authors considered the attitude dynamics of the central spacecraft, the elastic deformation of the tethers, and the rigid-flexible coupling between the tethers and the spacecraft. The tether deformation was again described by the high-fidelity nodal position finite element method. Through a parametric analysis, the authors [91] showed that the deformation motion of the flexible tethers is responsible of the onset of disturbance torques acting on the central spacecraft, which produce the tension fluctuations and the undesired fluctuations of the E-sail attitude and spin rate. In particular, they also addressed the controllability of the E-sail spin rate by applying simple feedback control torques at the central spacecraft alone or at the central spacecraft and remote units simultaneously [91]. It was shown that the spin rate can only be controlled at the remote units with finite control inputs.

6. Heliocentric mission scenarios

In the context of heliocentric mission scenarios, the use of reaction engines could limit the spacecraft maneuvering capabilities due to the finite amount of available propellant or to other complications such as the narrow length of launch windows or the need for gravity assist maneuvers, which are often essential to reduce the propellant consumption. For this reason, propellantless and continuous-thrust propulsion systems represent an interesting alternative, especially when high-energy transfers or long-term deep space missions have to be accomplished. In this regard, according to the mass budget model proposed by Janhunen et al. [28], the E-sail appears to be a promising propulsion system for a wide class of deep space missions with payloads in the range 30–1000 kg, which require a characteristic acceleration up to about $3\,\mathrm{mm/s^2}$.

The literature about E-sail-based heliocentric missions is very extensive and demonstrates the versatility of such an innovative propulsion system in an interplanetary framework. In this context, Janhunen [92] proposed four different classes of potentially feasible heliocentric missions scenarios using an E-sail as a primary propulsion system. A first class, which is of great scientific interest and represents a challenging technological issue, is the exploration of the interstellar space, beyond the heliosphere. A second group of potential scenarios consists in a rapid flyby mission towards a target in the Solar System, such as the countless objects belonging to the Kuiper belt that have never been closely observed. A third case is the positioning of a spacecraft at an artificial Lagrange point for solar wind monitoring purposes, in order to get early warnings of possible solar storms [93]. The orbital maintenance of a spacecraft at that position is impossible without the use of a continuous thrust propulsion system. The fourth class of E-sail-based scenarios includes other missions in the inner Solar System (towards the Sun, to an inner planet, or an asteroid), which would certainly require longer flight times than the same missions enabled by a chemical thruster option, but would have the advantage of not requiring any propellant to be flown. All those cases and many others have been extensively studied over the last decade with either numerical or semi-analytical approaches and with increasingly accurate thrust models that take into account new experimental or numerical evidences; see Section 3.1. The remainder of this section is devoted to a general survey of the heliocentric scenarios that have been investigated over the past 15 years to get a comprehensive overview of the E-sail potentialities.

To that end, it has been estimated that a spacecraft with a total mass of 100 kg, equipped with 100 tethers of 10 km each, may undergo a propulsive acceleration of up to 1 mm/s^2 [56].

The first class of potential scenarios identified by Ref. [92] concentrates on the exploration of the outer Solar System, while the second one involves rapid flyby missions with a distant target celestial body. Since these cases do not show substantial differences and are often analyzed together, the following discussion concentrates on the achievement of a large heliocentric distance and on flybys with celestial bodies in the outer Solar System; see Fig. 19. In this context, Mengali et al. [94] dealt with a number of minimum-

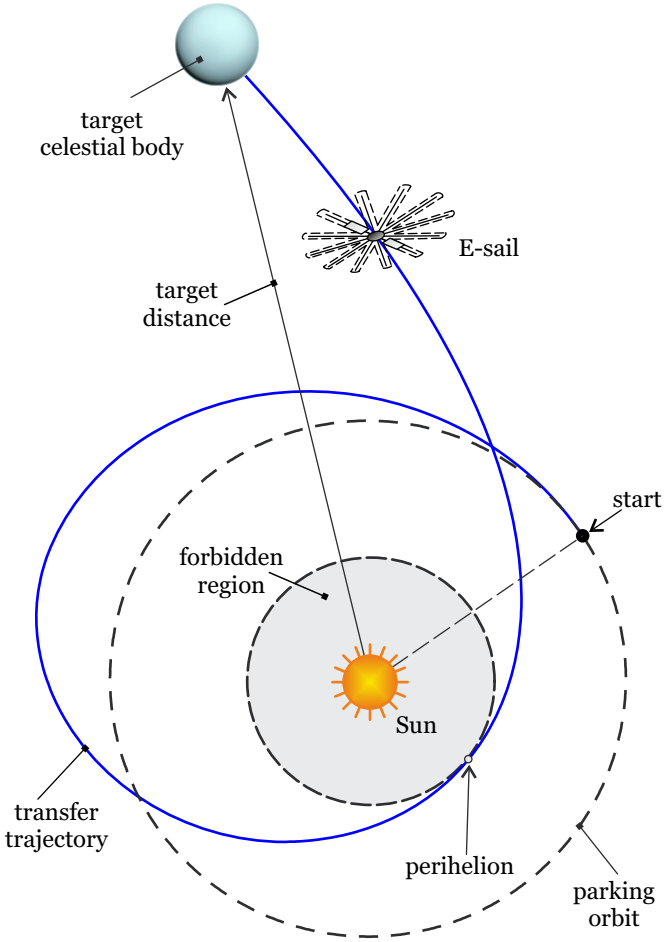

Figure 19: Typical E-sail transfer trajectory in flyby missions with a distant celestial body.

time transfer trajectories such as the achievement of the escape conditions from the Solar System or the accomplishment of a flyby with Neptune and Uranus. In particular, Uranus was chosen as the target planet also in Ref. [95], where the authors established that an E-sail capable of providing a thrust up to 0.5 N can boost a 550 kg spacecraft to perform a fast flyby with Uranus in less than 6 years (in this case, the corresponding characteristic acceleration is approximately equal to 0.9 mm/s^2).

The achievement of escape conditions from the Solar System was studied in Ref. [96], in which Quarta and Mengali analyzed a mission towards the heliopause using a time-optimal approach. The minimum flight time required to reach a given heliocentric distance or a given hyperbolic excess speed was estimated as a function of the characteristic acceleration. The authors [96] showed that it is sometimes convenient for the E-sail to approach the Sun in the initial transfer phase in order to exploit the greater propulsive acceleration magnitude that occurs due to the increase in solar wind electron density; see Fig. 19. This strategy resembles the solar photonic assist maneuver, which was suggested for a solar sail to gain orbital energy [97]. A medium performance E-sail may reach the distance of 100 au from the Sun within about 15

years, a result that confirms the previous estimates made by Janhunen [92]. In their calculations, Mengali et al. [94, 96] used the early thrust vector model in which the E-sail propulsive acceleration magnitude scales with the distance from the Sun as $r^{-7/6}$ and is unaffected by the sail attitude. This issue has been revised by most recent works, such as the study by Huo et al. [98], who analyzed E-sail-based missions to the heliosheath nose and to the heliopause nose by minimizing the total flight time required to reach a given target position in the Solar System. In this case, the authors took into account the plasmadynamic simulations carried out by Janhunen [58], according to which the E-sail propulsive acceleration magnitude varies as the inverse distance from the Sun, while its decrease with the sail pitch angle is again neglected. The numerical simulations presented in Ref. [98] show that an E-sail with performance consistent with the current technological level may reach a solar distance of 100 au within 23 years. Figure 20 shows the first part of a typical transfer trajectory towards the outer Solar System of a high performance E-sail with $a_c = 2\,\mathrm{mm/s^2}$, when the minimum Sun-spacecraft allowed distance is 0.5 au.

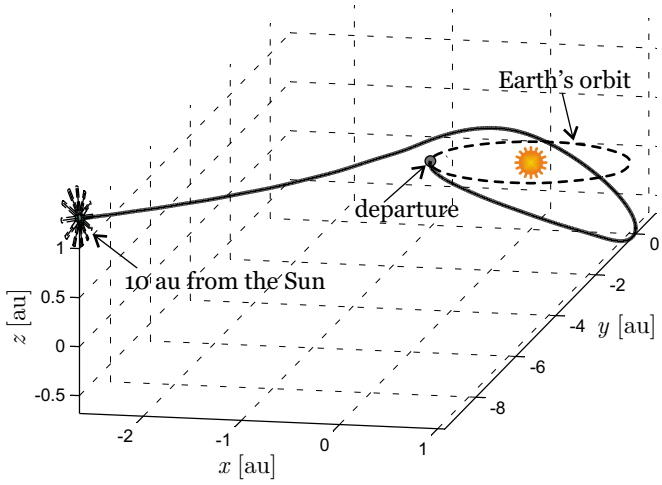

Figure 20: First part of transfer trajectory towards outer Solar System of a high performance E-sail. Adapted from Ref. [98].

The more refined mathematical model discussed in Ref. [62] was used by Bassetto et al. [84] to estimate the flight times necessary for an E-sail to reach the solar distance of 100 au as a function of its characteristic acceleration. In that case, the authors [84] used a locally optimal formulation in which the sail attitude is chosen such as to maximize the instantaneous variation of the specific mechanical energy of the spacecraft orbit. The obtained results show that 23 years are necessary when the characteristic acceleration is $1\,\mathrm{mm/s^2}$, while the flight time reduces to only 12.5 years provided the characteristic acceleration is doubled. The results discussed so far represent a significant improvement over the traditional approaches (i.e., chemical propulsion combined with solar and planetary gravity assists), which allow the heliopause to be reached within 25–30 years at least, thus suggesting an E-sail-based spacecraft to be a promising candidate for exploring the outer regions of the Solar System.

The third group of potential mission scenarios proposed in Ref. [92] consists of the generation of an artificial Lagrange point in the circular restricted three-body problem (CRTBP) sketched in Fig. 21, by exploiting the continuous thrust generated by an E-sail without consuming any propellant mass. An L_1-type artificial equilibrium point (AEP) could be used to provide an early warning in case of catastrophic solar events, while other AEPs would constitute privileged positions for the observation of celestial bodies in the inner Solar System. In this context, Aliasi et al. [99] discussed the achievement and the linear stability of an AEP in the Sun-[Earth+Moon] CRTBP in the case of a generalized sail, defined as a sail with a propulsive acceleration that scales as $r^{-\eta}$. In that model, the E-sail case corresponds to when $\eta = 1$. Later, the same authors extended the results to the elliptical restricted three-body problem [100]. The obtained results highlight that L_1-type AEPs are feasible for near- and mid-term technology levels but they are unstable points, while artificial triangular equilibrium points may be stabilized by suitably choosing their position. On the other hand, out-of-the-Ecliptic AEPs are more demanding to be maintained in terms of propulsive acceleration they require, while L_2-type points are unsuitable for an E-sail due to

the related eclipse conditions. For those reasons most of recent works have been concentrated on L_1-type AEPs. For example, Niccolai et al. [101] studied the E-sail-based generation of an L_1-type AEP in the Sun-[Earth+Moon] CRTBP and proposed a suitable control strategy for orbital maintenance while including the fluctuations of solar wind properties in the model; see Section 6.1. More recently, Wang et al. [102] extended the analysis to the case of a formation mission in the vicinity of an AEP, suggesting the use of a fault-tolerant control strategy that allows the desired configuration to be maintained.

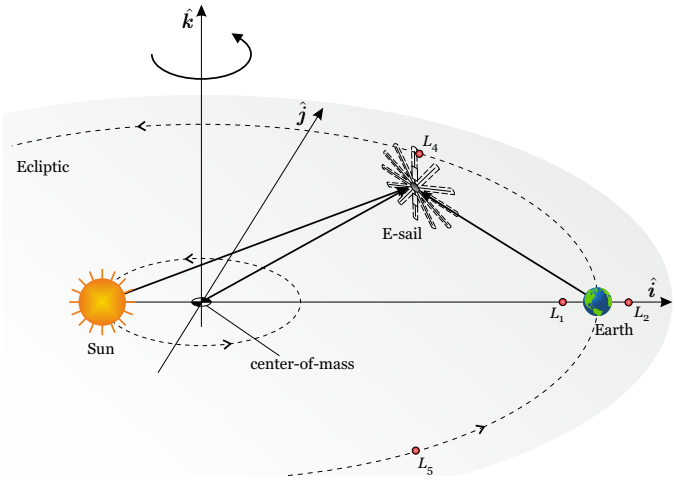

Figure 21: E-sail in the CRTBP.

The last group of potential E-sail-based mission scenarios consists in the deep space transfers and exploration of celestial bodies in the inner Solar System, including planets, near-Earth asteroids (NEAs), and comets. Most of the works that consider E-sail-based interplanetary transfers have already been mentioned in Section 5.1 when discussing the orbital control; see Refs. [62, 74, 75, 76, 77, 78] for indirect methods and Refs. [81, 82] for direct methods. In this regards, the most recent results are those provided by Huo et al. [78], who reappraised the performance of an E-sail-based spacecraft in an interplanetary transfer with ephemeris constraints towards Venus and Mars by applying the more recent thrust model of Eq. (8).

Many works dedicated to the E-sail technology propose missions towards targets that require long flight times, such as asteroids or comets, in order to exploit the benefits offered by the propellantless propulsion. For example, Quarta and Mengali [103] analyzed the E-sail performance in a mission scenario involving a rendezvous with all the potentially hazardous asteroids known at the time, a total of 1025 celestial bodies. Using a time-optimal approach and assuming a sail characteristic acceleration of $1\,\mathrm{mm/s^2}$, they showed that 137 asteroids may be reached in the first six months, while 67% of the total within one year flight [103]. Similar results are confirmed by Ref. [104]. Huo et al. [82] investigated an Earth-Ceres transfer, providing an estimation of the required flight time. A subsequent work [75] dealt with the problem of quantifying the minimum flight time necessary for an E-sail to perform a flyby with one of the two orbital nodes of a NEA. That study involved the whole population of known NEAs at the beginning of 2013 and showed that over 60% of NEAs can be reached within 100 days, while a flyby with the entire population is possible in less than 10 months assuming the characteristic acceleration is equal to $1\,\mathrm{mm/s^2}$. In Ref. [105] the authors evaluated the transfer times required to accomplish a mission towards the NEA 1998 KY26. The minimum flight times are shown to be inversely proportional to the characteristic acceleration when the latter is greater than $0.3\,\mathrm{mm/s^2}$ [105]. Huo at al. [83] estimated the E-sail performance in an exploration mission towards the asteroid Ceres using a refined thrust vector model in which the thrust modulus and its direction are functions of the spacecraft attitude according to the polynomial expressions proposed by Yamaguchi and Yamakawa [60]. As expected, the minimum flight times are longer than that obtained with the simplified thrust vector model.

A transfer from the Earth to the comet 67P/Churyumov-Gerasimenko (the target of the European Rosetta mission) was analyzed by Quarta et al. [77] by looking for the optimal launch windows as a function

of the spacecraft characteristic acceleration. The authors [77] also performed a mass breakdown analysis of the spacecraft, based on the actual payload mass of Rosetta and showed that, assuming a scientific payload mass of 30 kg and a total in-flight mass of 105 kg, the minimum ephemeris-free flight time is 3.7 years when the characteristic acceleration is 0.4 mm/s^2 (obtained with 12 tethers, each one having a length of 6.1 km). The E-sail optimal transfer trajectory related to that scenario is shown in Fig. 22.

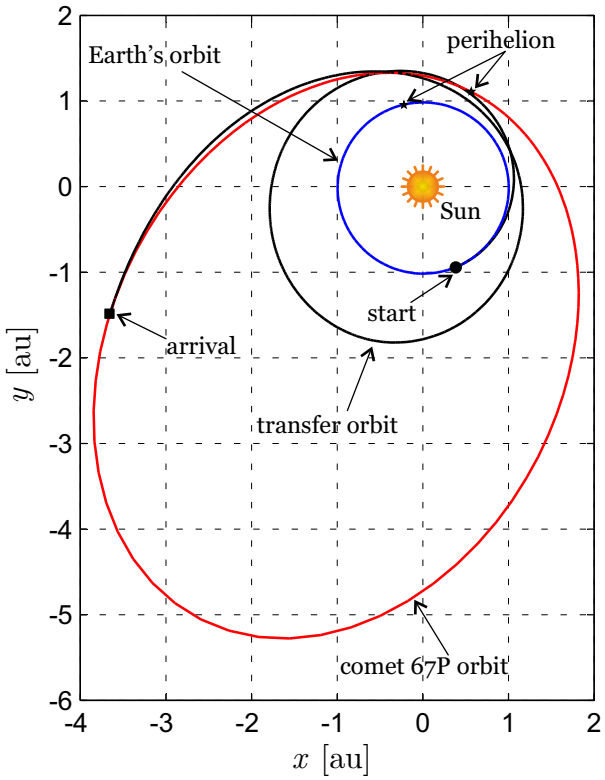

Figure 22: Ecliptic projection of the optimal transfer trajectory towards comet 67P/Churyumov-Gerasimenko. Adapted from Ref. [77].

Yamaguchi and Yamakawa [106] proposed the use of an E-sail-based spacecraft to deflect a fictitious asteroid from an Earth collision trajectory. Assuming that such an asteroid, with a mass of one million tons, is identified 15 years before its impact with the Earth, the authors [106] concluded that an E-sail-based spacecraft with a characteristic acceleration of 0.5 mm/s^2 and a total mass of 1000 kg can successfully deflect it. Bassetto et al. [84] analyzed the locally-optimal transfers towards the comets 67P/Churyumov-Gerasimenko and 1P-Halley under the assumption of equipping a spacecraft with an E-sail able of providing a characteristic acceleration of 1 mm/s^2.

Finally, Quarta et al. [76] analyzed transfer orbits within the Sun-[Earth+Moon] system of an E-sail by modelling the planetary system through the CRTBP. Using an indirect approach, the authors [76] dealt with minimum time trajectories between different equilibrium points and tested the effectiveness of such a propulsion system in the context of a tour through a subset of natural Lagrange points.

The results discussed by the previous papers clearly show the flexibility of an E-sail and its capability of reaching a wide range of targets in the inner Solar System, including planets, asteroids, and comets. Even though the necessary transfer times are usually longer than that obtainable with conventional thrusters, the cost savings due to the propellantless technology and the reasonable flight times could justify the choice of an E-sail-based spacecraft when dealing with conventional deep-space transfers in the inner Solar System.

The mission scenarios analyzed in Ref. [92] do not cover all the potentialities of such a propulsive system. Other innovative missions may be envisaged thanks to an E-sail, including the generation and the maintenance of displaced non-Keplerian orbits (DNKOs) [107]. The name comes from the fact that the orbital plane of a DNKO does not pass through center of mass of the primary. Due to this peculiarity,

these orbits are useful for the observation of the polar regions of the Sun or of a planet. With reference to DNKOs maintained by an E-sail, Ref. [107] discusses the thrust vector requirements in terms of magnitude and direction for a given Sun-spacecraft distance, elevation angle (the angle between the Sun-spacecraft position vector and the ecliptic), and angular velocity of the spacecraft along the DNKO. The same scenario was then again analyzed by Niccolai et al. [86, 108], who revisited the past results using a more refined mathematical model for describing the E-sail propulsive acceleration vector as a function of the sail plane attitude. Moreover, Refs. [86, 108] also presents a linear stability analysis of DNKOs and concludes that these orbits are unstable when the elevation angle exceeds about 20 deg. These results were extended in Ref. [109] to the case of elliptic DNKOs, whereas Pan et al. [110] analyzed the linearized relative motion and control of an E-sail operating in formation flight around a heliocentric DNKO. Wang et al. [111] presented a geometrical methodology for analyzing the formation flying problem of E-sails operating in elliptical DNKOs. In particular, the authors [111] investigated the relative motion of two E-sails (a chief and a deputy), which are travelling along two slightly different DNKOs. The paper reports a geometrical solution in terms of relative displaced orbital elements and finds an analytical solution to describe the bounds of relative motion when the DNKOs are nearly circular. A companion paper [112] discusses the control strategy (closely related to the formation structure) required for the deputy to track a prescribed trajectory relative to the chief by suitably adjusting its attitude and characteristic acceleration. In this context, Pan et al. [110] also performed a linear stability analysis of the relative motion and identified three categories of relative trajectories, according to whether the relative orbit is stable, unstable or locally unstable, the latter corresponding to an instability in the along-track direction. Finally, they proposed two effective feedback control strategies for stabilization: the former aimed at changing the topology of the relative motion to remove the instability caused by the presence of positive real eigenvalues, the latter aimed at maintaining the stability in the along-track direction [110].

A problem similar to the generation of a DNKO is given by the maintenance of a heliostationary condition. Actually, such a scenario represents a very challenging technological issue for an E-sail since the achievement of a heliostationary condition requires a high-performance propulsion system, well beyond the current technology level of an E-sail. Moreover, since the heliostationary condition is known to be unstable [86], a small error in the orbit insertion causes the spacecraft to move away from the prescribed reference position. Nevertheless, Bassetto et al. [65] proposed a feedback control system capable of stabilizing the dynamics of a spinning E-sail around a heliostationary position at a distance of one astronomical unit from the Sun. The control was obtained by adjusting the characteristic acceleration through a suitable modulation of the tether electrical voltage with a proportional or proportional-derivative control law. In their analysis [65], the authors employed approximate expressions for the thrust and torque vectors starting from the mathematical model described in Ref. [46] and discussed the effects of the propulsive torque on the rotational stability using a linearized approach.

More recently, the E-sail was proposed as a primary propulsion system for performing heliocentric phasing maneuvers by Mengali et al. [113], who studied the repositioning problem of a spacecraft along a circular working orbit for different values of characteristic acceleration and phasing angle. The assumption was made that the E-sail can be controlled by varying its attitude relative to the Sun and by switching the electron gun off to obtain coasting arcs. The optimal drift, which in principle can be forward or backward, was calculated as a function of the final azimuthal position by numerically determining the corresponding minimum flight times through an indirect approach. The same optimization method and control strategy were also adopted by Niccolai et al. [114], who analyzed the possibility of using an E-sail to deploy a constellation of small satellites on the same working orbit, also providing a semi-analytical expression of the required flight time as a function of the characteristic acceleration and the number of deployed satellites. Finally, Bassetto et al. [115] used a totally different approach, in which the E-sail provides a purely radial thrust along the whole transfer [116]. In that case, the trajectory analysis was obtained by reducing the problem to the dynamics of an equivalent nonlinear oscillator with a single degree of freedom by means of a suitable change of variable, following the approach used by Quarta and Mengali [117]. In particular, Bassetto et al. [115] found out an analytical relationship between the sail characteristic acceleration and the feasible phasing angle in the case of a low-performance E-sail.

A promising (albeit futuristic) E-sail-based scenario was first hypothesized by Janhunen et al. [118] in 2015. The authors suggested the use of a combination of E-sail technology with asteroid mining to provide water and synthetic cryogenic rocket fuel, thus promoting a continuous bidirectional traffic between Earth

and Mars. A further long-term technology level is represented by the exploration of other stellar systems, as proposed within the Project Dragonfly conducted by the Initiative for Interstellar Studies. So far, the best candidate propulsive technology for performing such an ambitious objective seems a laser photonic sail, but Lingam and Loeb [119] have recently proposed the E-sail as a valid alternative.

In principle, an E-sail could be combined with another propulsion system to increase its performance. For example, Quarta et al. [74] analyzed the performance of a hybrid arrangement, constituted by a chemical thruster and an E-sail, in the case of a two-dimensional interplanetary transfer. In this context, the chemical propulsion should be used during the escape phase from the Earth and the capture by the target planet, while the rest of the transfer should exploit the thrust provided by the E-sail. Using the hyperbolic excess speed as an input parameter in the simulations, the authors [74] related the minimum flight time with the total velocity variation required by the chemical thruster to accomplish the mission. Within the context of the Project Dragonfly, Perakis and Hein [120] proposed a novel concept for decelerating a probe during an interstellar mission by combining a magnetic sail [6], which is more effective at high velocities, with an E-sail, which has better performance at low speeds. According to the authors [120], the hybrid system would approximately require 29 years for decelerating an interstellar probe from 15000 km/s (about 5% of light speed) to a typical interplanetary-transfer velocity (on the order of few tens of kilometers per second), whereas the E-sail (or the magnetic sail) alone would take about 35 years (or 40 years).

6.1. Environmental uncertainties

Most of the analyses discussed so far on E-sail-based missions assume that the propulsive acceleration generated by the E-sail is precisely known and that it may be calculated using the reference values of the solar wind parameters, which are assumed to be stationary. Using this approach, the propulsive acceleration only depends on the Sun-spacecraft distance, the E-sail design characteristics, and its attitude. Unfortunately, the actual situation is more complex.

In fact, the data collected by several space missions such as Voyager [121], Ulysses [122], and ACE [123] show that the plasma parameters (in particular, the bulk speed and the plasma density) undergo significant and chaotic temporal fluctuations, the magnitudes of which are comparable to their mean values. Moreover, variations of plasma properties have also been recorded as a function of the heliocentric latitude. Those spatial variations may be neglected in a preliminary mission design phase because the plasma density variation roughly counterbalances the bulk speed changes. This results in a near constant value of the solar wind dynamical pressure, which ultimately affects the E-sail thrust generation. However, *in-situ* observations suggest that the solar wind property fluctuations must be properly taken into account in the design of an E-sail trajectory and that a suitable control strategy is probably required to counteract these environmental uncertainties.

The impact of the actual solar wind plasma properties on an E-sail trajectory was first studied in 2009 by Toivanen and Janhunen [124], who considered an Earth-Mars transfer as a reference mission scenario. To simulate the effects of fluctuating solar wind properties on the actual E-sail interplanetary trajectory, the authors [124] numerically integrated the dynamical equations of motion using the historical plasma properties retrieved by the OMNI database[1] (spacecraft-interspersed, near-Earth solar wind data). In that study [124], the temporal fluctuations are counteracted with a simple control system that adjusts the tether voltage in response to environmental variations. More precisely, the voltage is increased (or decreased) when the instantaneous solar wind velocity measured by an onboard sensor is smaller (or larger) than the corresponding value calculated at the same time instant on the optimal trajectory. The analysis proposed in Ref. [124] also accounts for a saturation constraint $V < V_{\max}$ and a fixed step-like variation between the i-th and the $(i+1)$-th time step, that is, $V_{i+1} - V_i = \pm V_{\mathrm{st}}$. In their study, the authors [124] assumed $V_{\max} = \{10,\ 40\}$ kV and $V_{\mathrm{st}} = V_{\max}/12$, thus obtaining very promising numerical results in terms of targeting accuracy.

Although this interesting work [124] adopts the E-sail thrust model in which the propulsive acceleration scales with the distance from the Sun as $r^{-7/6}$ (see Eq. (1)), the proposed approach is rather sophisticated in terms of parameters it contains. Moreover, the fact of containing many aspects of the plasma interactions helps to mitigate the effects of plasma property fluctuations on the interplanetary trajectory. In fact, an

[1] OMNI data may be retrieved at https://omniweb.gsfc.nasa.gov/

increase of plasma density tends to increase the thrust magnitude, but it also decreases the electron Debye length (which scales as $n^{-1/2}$), thus reducing the overall impact on the thrust vector. On the other hand, an higher density n also increases the gathered electron current, thus reducing the E-sail performance parameter by affecting the tether voltage. Likewise, an increase in solar wind bulk speed tends to increase the thrust magnitude, but it also allows the ions to deeper penetrate into the E-sail electric field, thus limiting the thrust increase. These feedback and rather complex phenomena, along with the previously discussed simple control law, seem to effectively contribute to counteract the solar wind plasma fluctuations.

More recently, a similar analysis was performed by Wang and Bian [125], who used the same thrust model and the same historical solar wind data as that of Ref. [124]. However, their control strategy is significantly different, because Wang and Bian [125] proposed a composite control law, which combines a disturbance observer-based sliding mode control with hierarchical sliding surfaces. In that approach, only the saturation constraint is enforced, while the voltage variation constraint is removed. The latter assumption is justified by the fact that the characteristic times of tether voltage variations are significantly smaller than the typical flight times. In particular, the control law of Ref. [125] is applied to an Earth-Mars transfer with very promising results, since the controlled E-sail is able to track the reference trajectory with good accuracy.

The same problem was analyzed by Niccolai et al. [126, 127] assuming that the E-sail thrust magnitude scales with the heliocentric distance as $1/r$ (see Eq. (8)) but neglecting all of the complex feedback phenomena discussed in Ref. [124]. The analysis proposed in Refs. [126, 127] is not based on historical solar wind data, but uses an elegant stochastic approach. More precisely, the solar wind dynamical pressure p is modelled as a random variable, which therefore takes a different value at each time step, with a given probability density function based on experimental measurements. In that context, p is described by a gamma distribution with mean value and standard deviation equal to those obtained by experimental measurements, so that it is reconstructed to match all the statistical properties of OMNI data. The effect of the random values of the solar wind dynamical pressure on the E-sail heliocentric distance r is estimated with a generalized Polynomial Chaos procedure [128]. In particular, the output r is projected over an orthogonal polynomial base, the elements of which are functions of the random input variable p. The infinite summation is then truncated at a certain order and the coefficients are evaluated numerically.

This procedure provides an estimate of the uncertainty of r as a function of p and the numerical results clearly show that a control system is required for targeting the final state. In this context, the authors [126, 127] adopted a control law similar to that of Ref. [124] with a saturation constraint $V < V_{\max}$ and a maximum step variation between the i-th and the $(i+1)$-th step, that is, $|V_{i+1} - V_i| \leq V_{\rm st}$. The effectiveness of such a refined control law in maintaining the working orbit was tested in some potential heliocentric mission scenarios, including displaced non-Keplerian orbits [126, 127], interplanetary transfers [129], and generation of artificial Lagrange points [101]. The numerical simulations show how the saturation constraint is less critical than that involving the maximum voltage variation, even though the latter may actually be removed or significantly relaxed.

The results discussed in this section highlight that the fluctuations of solar wind properties is a relevant issue for an E-sail-based heliocentric scenario. However, even a simple control law could guarantee a fairly accurate orbital maintenance, assuming the electrical voltage variation to be sufficiently fast. When an accurate orbital maintenance is required, a more complex control law is necessary such that the error between the instantaneous and the target state may in principle be canceled out. In practice, the physical mechanisms that tend to reduce the oscillations of the E-sail thrust should also be accounted for.

7. Plasma brake concept: a geocentric application of the E-sail technology

An E-sail propulsion system is, in principle, a large and complex space structure, and its use in interplanetary missions requires that some relevant issues are properly addressed, including the implementation of a reliable deploying strategy, the control of tether oscillations, and the response to environmental uncertainties. A simpler propulsive concept based on the same working principle, the plasma brake, has been developed starting from the preliminary studies made on an E-sail with negative polarity. The plasma brake has been conceived for a geocentric mission scenario, and this mechanism could represent a good and inexpensive option for deorbiting small- or medium-size satellites from a LEO. Accordingly, the plasma brake can contribute to reduce the overpopulation of this orbital range [130] without generating many orbiting

debris, even in the event of spacecraft collision. The origin of the plasma brake concept, its main features and the possible applications to future space missions will now be revised.

7.1. E-sail with negative polarity

Although in the mission scenarios discussed so far the E-sail tethers are assumed to be positively-charged, an E-sail with a negative polarity was also studied by Janhunen [131] in 2009. The main advantage of this arrangement is in the fact that, in this case, the solar wind ions are not trapped by the potential structure because their thermal speed (about 40 km/s) is much lower than the solar wind bulk velocity (roughly 400 km/s). The opposite occurs in a positively-charged E-sail, where some electrons (with a thermal speed of about 1600 km/s) could in principle get trapped in the potential structure, thus significantly decreasing the overall E-sail performance.

In Ref. [131], the thrust magnitude F per unit of tether length (i.e., $\mathrm{d}F/\mathrm{d}x$) in the negative polarity case is approximated as

$$\frac{\mathrm{d}F}{\mathrm{d}x} \simeq 1.72\, m_i\, n\, v_{\mathrm{sw}}^2 \sqrt{\frac{\epsilon_0\, |V|}{n\, e_e}}\, \exp\left(-\frac{m_i\, v_{\mathrm{sw}}^2}{2\, e_e\, |V|}\right) \tag{47}$$

where m_i is the ion mass, while the other quantities are defined as in Section 3.1. In particular, the effective Debye length of a negatively charged E-sail is

$$\lambda_{De}^{\mathrm{eff}} = \sqrt{\frac{\epsilon_0\, |V|}{n\, e_e}} \tag{48}$$

which gives a (rather large) value of about 87 m when $|V| = 1\,\mathrm{kV}$ and $n = n_{\oplus}$.

To assess the feasibility of an E-sail with negative polarity, it is necessary to first calculate the ion current gathered from the surrounding plasma. The analysis discussed by Janhunen [131] provides an estimation of the main sources of the ion current. The results highlight that the thermal ion current (generated by the thermal motion) and the photoelectron current (generated by the solar UV radiation) are much smaller than their corresponding values in the case of an E-sail with positive polarity. However, the electron field emission current is more difficult to evaluate with ground experiments, since the presence of two electrodes could generate feedback phenomena between the cathode and the anode, whereas in the deep space the anode is constituted by the solar wind plasma.

Preliminary numerical simulations show that the field emission current is relevant for an E-sail with negative polarity, especially in regions with impurities or dust contamination, so that the maximum allowable tether voltage $|V|$ is upper limited to values smaller than about 1.5 kV. This suggests that an E-sail with negative polarity could generate a smaller thrust magnitude and have a smaller characteristic acceleration a_c when compared to an E-sail with positive polarity and same dimension and mass. Moreover, the maintenance of the negative charge needs an ion gun, which is a more complex component than the electron gun sketched in Fig. 14, since it basically consists of an ion engine that requires some propellant (that is, ionizable gas) to work.

Further analyses and simulations performed by Janhunen [58] show that the number of trapped electrons in an E-sail with positive polarity is much smaller than those initially estimated, so that the main advantage of an E-sail with negative polarity for deep space missions is significantly reduced. Nevertheless, the analysis conducted on E-sails with negative voltage has laid the foundation of a different concept, the plasma brake, with very interesting geocentric applications.

7.2. The plasma brake concept

A plasma brake is a simple and propellantless deorbiting device for satellites in a LEO, proposed by Janhunen [57] in 2010. It consists of a single negatively charged tether that is unreeled by an orbiting satellite to generate a drag force, referred to as Coulomb drag, due to the electrostatic interactions between the tether and the charged particles in the ionosphere plasma; see Fig. 23.

The Coulomb drag provided by the tether enables the spacecraft to deorbit in a time interval that complies with the Inter-Agency Space Debris Coordination Committee (IADC) guidelines [133, 134], that is, less than 25 years after the end of the operational life. The increase of plasma density in the Earth's ionosphere, which is greater than that in the deep space by about a factor 10^4, is able to compensate for the

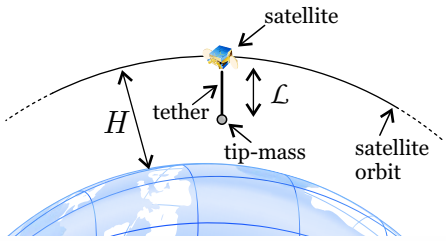

Figure 23: Basic scheme of the plasma brake concept proposed by Janhunen [57]. Adapted from Ref. [132].

reduction of the plasma-tether relative velocity (on the order of 7.5 km/s), when compared to a typical value of 400 km/s for the interplanetary solar wind case. This aspect allows a sufficient net force to be generated, even considering the limitations on the maximum value of the tether voltage to avoid problems with the field emission current [57].

The main advantage of using a negatively charged tether for the plasma brake concept is in the fact that, unlike the deep space applications, in this case an ion gun is not necessary to maintain the tether voltage [57]. In fact, a conductive spacecraft naturally acquires a negative charge due to the higher thermal mobility of electrons compared to that of ions. In particular, the negative current I_e collected by the spacecraft main body may be estimated as

$$I_e = n\, e_e\, A \sqrt{\frac{k_B\, T_e}{2\,\pi\, m_e}} \tag{49}$$

where T_e ranges between 1000 K and 2000 K (the typical electron temperatures in the Earth's ionosphere) and A is the spacecraft conductive area. Typical values of the electron current per square meter of conductive area provided by Eq. (49) are on the order of 0.3–12 $\mathrm{mA/m^2}$, with a strong dependence on the surrounding plasma properties.

The ion current I_i gathered by the tether immersed in the ionosphere plasma can be estimated with the orbital motion limited theory [135], which models the tether as a cylindrical Langmuir probe and assumes the current to be constant along the cable, viz.

$$I_i = n\, e_e\, \mathcal{L}\, K_t\, r_w \sqrt{\frac{8\, e_e\, |V|}{m_i}} \tag{50}$$

For example, when $K_t \simeq 1$ (i.e., for a Heytether configuration; see Section 2.3), typical values of the ion current per tether length are on the order of 2–150 $\times\, 10^{-5}$ mA/m and, again, strongly depend on the surrounding plasma density.

Equations (49) and (50) may be used to assess the requirements of an ion gun because, as long as $I_i < I_e$ (an easy condition to fulfill, since the conductive area of the spacecraft is usually rather large), the presence of an onboard ion gun is actually not required. Moreover, Eq. (50) allows the required electric power P for maintaining the tether voltage to be calculated as

$$P = I_i\, |V| \tag{51}$$

which gives typical values of power consumption per tether length on the order of 0.25–25 mW/m. These results provide an estimation of the required power for a plasma brake device of about 70 mW for a 100 m long tether, assuming a voltage of $|V| = 1$ kV.

The Coulomb drag generated by a plasma brake may be estimated by applying the same procedure as that used to determine the thrust of an E-sail with negative polarity [131]; see Eq. (47). However, the expression (47) was later updated to get more accurate results in a geocentric mission case with a ionosphere environment [136]. In this context, assuming a constant drag per unit length and a Heytether structure, the

total Coulomb drag D is estimated as [136]

$$D = 3.864\,\mathcal{L}\,m_i\,n\,v_{\mathrm{rel}}^2\sqrt{\frac{\epsilon_0\,V^\star}{n\,e_e}}\,\exp\left(-\frac{m_i\,v_{\mathrm{rel}}^2}{2\,e_e\,V^\star}\right) \tag{52}$$

where v_{rel} is the spacecraft speed relative to the ionosphere, while the coefficient 3.864 is used instead of 1.72 (see Eq. (47)) to better fit the simulation results. Note that the electric potential $|V|$ in Eq. (47) is replaced in Eq. (52) by a modified potential $V^\star$, defined as

$$V^\star \triangleq \frac{|V|}{\ln\left(\lambda_{De}^{\mathrm{eff}}/r_w^{\mathrm{eff}}\right)} \tag{53}$$

where r_w^{eff} is the effective tether electric radius, which is defined in analogy with Ref. [55] as $r_w^{\mathrm{eff}} \triangleq \sqrt{b_t\,r_w}$, being $b_t \simeq 2\,\mathrm{cm}$ the total tether width and $r_w \simeq 25\,\mu\mathrm{m}$ the radius of the wires constituting the tether; see Fig. 10. Substituting the expressions of r_w^{eff} and $\lambda_{De}^{\mathrm{eff}}$ (see Eq. (48)) into Eq. (53) the result is

$$V^\star = \frac{2\,|V|}{\ln\left(\dfrac{\epsilon_0\,|V|}{n\,e_e\,b_t\,r_w}\right)} \tag{54}$$

Equations (52) and (54) allow the Coulomb drag generated by a plasma brake device to be estimated as a function of the tether characteristics ($|V|$, L_t, b_t, and r_w), the plasma properties (n_0 and m_i), and the relative velocity of the plasma with respect to the tether v_0, which coincides with the spacecraft orbital velocity in the ionosphere. The plasma parameters may be retrieved by the International Reference Ionosphere (IRI). The latter is a complex mathematical model that provides accurate estimations of the ionosphere properties, which was first proposed in the late seventies [137] and is periodically updated [138, 139, 140, 141, 142, 143]. Since the Coulomb drag estimated with Eq. (52) per tether length is about 40–200 nN/m, the plasma brake concept is especially suitable for small or medium satellites.

The Coulomb drag expression given by Eq. (52) allows the deorbiting time of a spacecraft in a LEO to be estimated by means of numerical integration of the equations of motion. In this context, Janhunen [57] simulated the deorbiting phase from a polar LEO of three spacecraft with different sizes (with total mass $m \in \{3,\,10,\,100\}\,\mathrm{kg}$) and equipped with three different plasma brake tethers (with $L_t \in \{0.7,\,1.2,\,7\}\,\mathrm{km}$ and $|V| \in \{0.15,\,0.5,\,1.5\}\,\mathrm{kV}$, respectively). The results show that the maximum required deorbiting time, corresponding to the highest initial altitude $H = 900\,\mathrm{km}$, is on the order of 500–540 days. Notably, in Ref. [57] an old estimation is used in Eq. (52), where the coefficient 3.864 is replaced by 1.72, which comes from the initial studies on E-sails with negative polarity in deep space [58]; see Eq. (47). However, a mistake in the expression of the Coulomb drag, where $|V|$ is confused with $V^\star$, was remarked in later works (see Ref. [136]) and the author pointed out that the two inaccuracies roughly cancel out.

A simpler and more handy approach for modelling the Coulomb drag is discussed by Orsini et al. [132]. In that analysis, the ion mass is assumed to be constant with $m_i = 16\,\mathrm{u}$, corresponding to atomic oxygen ions. In fact, the mean ion mass in the ionosphere is not constant, as can be observed from Fig. 24 that refers to a mean solar activity phase. However, the value of 16 u is acceptable for a preliminary estimation. The plasma density n is expressed with respect to a reference value $\widetilde{n}$ by means of the geopotential model, viz.

$$n\ = \widetilde{n}\,\exp\left\{-\frac{m_i\,g_0\,R_\oplus^2}{2\,k_B\,T_i}\left[\frac{H}{(R_\oplus+H)^2}-\frac{\widetilde{H}}{(R_\oplus+\widetilde{H})^2}\right]\right\} \tag{55}$$

where the tilde symbols denote quantities measured at a reference altitude $\widetilde{H}$. In Eq. (55), H is the spacecraft altitude, g_0 is the standard gravity, $R_\oplus$ is the Earth's mean radius, and T_i is the temperature of ions. The latter may be estimated by thermal equilibrium considerations, assuming it coincides with that of electrons and neutral particles, and assuming it is constant within the LEO range (a typical value of $T_i = 1011.5\,\mathrm{K}$ [144, 145] for the mean solar activity was used in the simulations of Ref. [132]).

The Coulomb drag at a generic altitude H is written as a function of the Coulomb drag at the reference

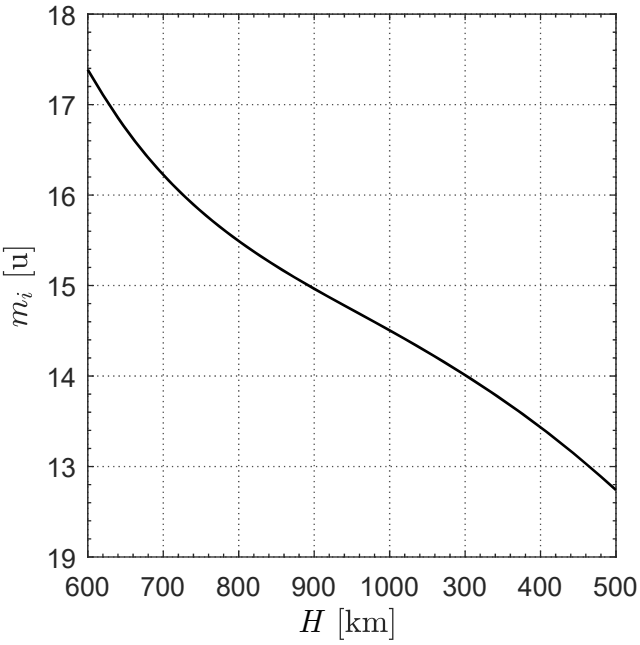

Figure 24: Mean molecular mass of ionosphere ions; a mean solar activity is assumed. Adapted from Ref. [132].

altitude by means of Eq. (52)

$$D = \widetilde{D} \sqrt{\frac{n}{\widetilde{n}}} \left(\frac{v_{\mathrm{rel}}}{\widetilde{v}_{\mathrm{rel}}} \right)^2 f_1 \left(v_{\mathrm{rel}} \right) \, f_2 \left(n, v_{\mathrm{rel}} \right) \, f_3 \left(n \right) \tag{56}$$

where the complete expressions of $f_1(v_{\mathrm{rel}})$, $f_2(n, v_{\mathrm{rel}})$, and $f_3(n)$ are rather involved and are not reported here for the sake of conciseness. Following the discussion of Ref. [132], the values of the three functions may be evaluated in the LEO range using the IRI values and taking $\widetilde{H} = 1000\,\mathrm{km}$. Orsini et al. [132] showed that the approximation $f_1 \times f_2 \simeq 1$ is very accurate for the whole LEO range. Moreover, f_3, which is greater than 1, is also close to 1 in the LEO range with an error below 10% when $H > 500\,\mathrm{km}$, so that the approximation $f_3 \simeq 1$ is both conservative and sufficiently accurate for a preliminary analysis. Finally, the squared velocity ratio in Eq. (56) may be estimated with the ratio of squared circular velocities at H and $\widetilde{H}$. The result, which ranges in the interval [0.91, 1.10], is again approximated with the unity. The latter assumption should be revised in case a spinning plasma brake tether is considered in place of a gravity-gradient stabilized configuration, to only account for the component of the ion flux perpendicular to the tether. From the previous considerations, according to Ref. [132], the variation of D in the LEO range is mainly caused by the variation of the plasma density, which is a function of the altitude only in a geopotential model; see Eq. (55). The resulting expression of D is

$$D = \widetilde{D} \, \exp\left\{ -\frac{m_i \, g_0 \, R_\oplus^2}{4 \, k_B \, T_i} \left[\frac{H}{(R_\oplus + H)^2} - \frac{\widetilde{H}}{(R_\oplus + \widetilde{H})^2} \right] \right\} \tag{57}$$

the only unknown of which is H. Accordingly, Eq. (57) allows the value of D to be calculated for any altitude H within the LEO range by using the IRI database to retrieve the plasma properties. The numerical simulations discussed in Ref. [132] highlight that this approximate method provides an estimation of the required deorbiting time for a spacecraft in a LEO with a maximum relative error on the order of 7% when compared to a numerical simulation based on the data from IRI. Moreover, the computational time saving is about two orders of magnitude. These results, which are adequate for preliminary design purposes, were later applied to analyze the dynamics of a spacecraft equipped with a plasma brake tether during the deorbiting

phase, with special attention to either the geocentric motion [146] or the relative motion with respect to a reference orbit [147] (in the latter case using the Hill-Clohessy-Wiltshire equations [148]).

While the previous approach for calculating the plasma brake-induced drag provides reasonable results for a preliminary mission analysis, more complex simulations are required for an accurate knowledge of the Coulomb drag generation. In particular, Ref. [132] neglects the solar activity variation and the effects of the magnetic field on the Coulomb drag. However, the solar activity level influences the plasma density, the presence of atomic oxygen, and the particle temperature, thus affecting the Coulomb drag generation through the terms n_0, m_i, and T_i; see Eq. (52). In fact, the effects of the solar activity on the drag expression were evaluated by Janhunen [149, 150], who estimated that the ratio of the drag corresponding to a solar maximum to the that generated at a solar minimum amounts to about 3.5. Although this difference is relevant and must be considered when estimating the decay profile, the deorbiting times provided by Refs. [57] and [132] for a mean solar activity are well below the limit of 25 years suggested by IADC. Finally, when one or more spinning tethers are used, the ion flux is not always perpendicular (or nearly-perpendicular) to the tether, and the required deorbiting time reduces. Again, the promising results of Ref. [132] suggest that this issue will not significantly affect a plasma brake-based deorbit. Therefore, the international guidelines are met even if the deorbiting phase takes place at a solar minimum.

The accuracy of Eq. (52) must be checked when the presence of the Earth's magnetic field is taken into account. An order-of-magnitude analysis is sufficient to conclude that the Lorentz force acting on the tether is negligible when compared to the electrostatic Coulomb drag due to the very small current flowing in the tether; see Eq. (50). However, the effect of the magnetic field on the plasma sheath and, therefore, on the drag generation predicted by Eq. (52), must be evaluated. In this regard, Janhunen [136] carried out some numerical simulations with an electrostatic kinetic particle-in-cell (PIC) model [151] and quantified the effects of varying the ion mass m_i and the ion temperature T_i. The obtained results suggest that an increase of ion temperature does not significantly affect the reliability of Eq. (52) and also provides a damping of the thrust oscillations. Simulations with different ion masses show a good agreement with Eq. (52), with a small underestimation of the Coulomb drag for lighter ions (such as helium and protons), possibly due to their reduced interaction with the plasma sheath. The most relevant discrepancies between the PIC simulations and Eq. (52) were found, as expected, by considering the magnetic field contribution. In particular, when the magnetic field lines are perpendicular to both the tether and the relative plasma velocity, their effect is negligible. On the other hand, field lines parallel to the plasma velocity and field lines parallel to the tether axis generate instability in the plasma sheath, with a thrust reduction on the order of 11% and 17%, respectively, compared to the values predicted by Eq. (52) for $|V| = 320\,\mathrm{V}$. When the voltage $|V|$ is increased, the detrimental effect of the field lines along the plasma velocity reduces, and even a small thrust increase takes place at $|V| = 800\,\mathrm{V}$, while the effect of field lines along the tether increases with a corresponding thrust reduction of about 27%.

In other words, Eq. (52) accurately predicts the Coulomb drag found in the PIC simulations, with the only remarkable exception constituted by the presence of a relevant magnetic field component along the tether. This situation does not occur in most low- or medium-inclination LEOs, whereas it is expected to increase the deorbiting time from polar or nearly-polar orbits. In any case, the IADC guidelines are fully satisfied by the deorbiting profiles of polar orbits discussed in Ref. [57]. Therefore, the plasma brake principle is an effective option to guarantee an autonomous decay of most satellites starting from a typical LEO, even accounting for the magnetic field effect.

7.3. Comparison with other deorbiting technologies

The estimated performance of a Coulomb drag-based deorbiting technology is now compared with other possible deorbiting options for a spacecraft in a LEO. To that end, in addition to the decay times, the main plasma brake characteristics must also be considered, including the total system mass and the required power consumption. Janhunen [57] provided a mass estimation of the three previously discussed plasma brake devices, with tether voltage $|V| \in \{0.15, 0.5, 1.5\}\,\mathrm{kV}$, tether length $\mathcal{L} \in \{0.7, 1.2, 7\}\,\mathrm{km}$, and total spacecraft mass $m \in \{3, 10, 100\}$. Assuming a Heytether structure, the results for the total plasma brake system mass are $m_{\mathrm{PB}} \in \{46, 84, 257\}\,\mathrm{g}$, including the tip mass. The required power, calculated with Eqs. (50) and (51), is $P \in \{0.035, 0.360, 11\}\,\mathrm{W}$ for a mean solar activity. Finally, the total spacecraft conductive area required to maintain the negative charge of the tether without an ion gun is $A \in \{0.12, 0.38, 3.8\}\,\mathrm{m}^2$. These are all small values if compared to the spacecraft size.

Kvell et al. [152] made a comparison between plasma brake and conventional propellant-based deorbiting devices, that is, chemical or electric thrusters. A deorbiting phase with impulsive maneuvers generated by a chemical engine is obviously very fast, with typical decay times of about 1 hour, but a significant amount of propellant must be stored onboard until the end of the operative life. Instead, using a spacecraft equipped with an electric thruster, the total required mass is about 10 times smaller, but the amount of necessary power increases up to some hundreds of watts and the required deorbiting time becomes on the order of 25 years, at the limits of IADC guidelines. As already discussed, the plasma brake technology enables an orbital decay from a LEO within a time span on the order of 1–3 years for most small satellites. This performance may be achieved with a smaller power consumption compared to the electric propulsion case and a significant mass saving compared to the chemical propulsion option.

Other propellantless technologies exist that enable a spacecraft to deorbit from a LEO. For instance, an augmented drag device such as a drag sail [153] may be exploited for an orbital decay in a very short time, although the complexity of the sail structure and the issues associated with the sail development are relevant. Hybrid solutions have also been proposed [32], which exploit both the augmented aerodynamic drag and the generation of a Coulomb drag. Another tether-based propellantless deorbiting technology is the electrodynamic tether [17, 154, 155]. The latter generates a Lorentz drag by exploiting the electrodynamic interaction between a large current flowing in the tether and the lines of the Earth's magnetic field. Such a drag generation system is very promising and seems to be very effective for large satellites, possibly outperforming the plasma brake concept in terms of drag generation, as discussed in Ref. [156]. However, as long as small or medium satellites are concerned, the comparison discussed in Ref. [156] must be reconsidered to a large extent, mainly because they require shorter tethers that make the plasma brake option competitive with the electrodynamic tether. In addition, an electrodynamic tether requires a power consumption (and, consequently, a power generation system) that is one order of magnitude larger than that necessary for a plasma brake device [57]. Finally, electrodynamic tethers are thicker than plasma brake tethers, thus increasing the collision risk during the deorbiting phase.

In conclusion, the plasma brake technology probably outperforms most of the available deorbiting technologies in terms of decay time and system simplicity. The most notable exception is the electrodynamic tether, which seems more suitable than a plasma brake to deorbit large satellites. However, note that these considerations are still preliminary since they require to be validated through suitable *in-situ* measurements and mission tests.

7.4. Test missions

Due to its design simplicity and applicability to a LEO mission, the plasma brake concept has been chosen as a technology demonstrator of the electric sail working principle. The first test was attempted with the Estonian student satellite ESTCube-1, the design of which was lead by the University of Tartu, Estonia, and supported by ESA. ESTCube-1 was a 1U CubeSat with a mass of about 1 kg [157], equipped with an Heytether of 10 m, negatively charged to maintain a negative potential of $|V| = 500$ V [158]. The spacecraft was launched on May 7, 2013 onboard a Vega rocket, but unfortunately a failure of the tether unreel mechanism occurred during the launch phase, and the tether experiment did not take place. Later, ground tests showed that the piezoelectric motor (see Section 2.2) was damaged by the launch phase vibrations [159], so that the failure was not due to an intrinsic flaw of the plasma brake technology, but may be solved with some spacecraft design improvements [160].

The lessons learned from the ESTCube-1 failure have led to the design of Aalto-1, a Finnish 3U-CubeSat with a weigh of about 4 kg, the design of which was guided by the Finnish Meteorological Institute. Aalto-1 was equipped with a scientific observation payload and another plasma brake experiment [150, 161]. The latter was constituted by four tethers with a total length of 100 m and was expected to be deployed through the centrifugal force generated by the spinning satellite [162]. The experiment was planned to take place in different phases [39], the first one involving a positive polarity and a total tether length of 10 m only. The reason for such a requirement was that the onboard electron gun should be capable of removing electrons gathered by the tether. The negative polarity case was planned to be tested on the total tether length, because in that case the spacecraft acts as an electron collector, thus maintaining the negative charge of the tether. The payload of the plasma brake experiment was successfully ground-tested in thermal-vacuum prior to the system level tests [163]. In particular, vibration tests were made to qualify the mechanical components, the reel Printed Circuit Board (PCB), and the reel motor. Praks et al. [163] noted that the high voltage

sliders dug two dents on the slip ring that prevented the reel from rotating. They then inserted simple resistor-based launch locks to the bottom side of the reel PCB in order to keep the sliders separate from the slip ring during the launch. They also carried out high voltage tests and analyzed the tether unreeling mechanism in order to fix the minimum centrifugal force required for the tether deployment. It is worth highlighting that the Aalto-1 flight model hardware had to be delivered just four months after ESTCube-1 failure. The shortage of diagnostic data did not give the project team enough time to correct the issues emerged from the previous mission [164]. However, as pointed out in Ref. [164], a number of diagnostic devices were inserted onboard, in order to gather a large amount of data from the plasma brake experiment attempt. Aalto-1 was launched on June 23, 2017 and after one year of technical issues (mainly concerning the communication subsystem) it started the planned remote sensing operations. Unluckily, after some encouraging preliminary tests, the deployment of the plasma brake tether did not occur, probably due to a failure of the boost converter that was supposed to maintain the nominal working voltage of the unreeling mechanism motor [164].

The ESTCube project, which led to the ESTCube-1 mission, is currently ongoing with the aim of launching ESTCube-2. ESTCube-2 is a 3U-CubeSat that should provide in-orbit measurements of Coulomb drag [44]. To this end, ESTCube-2 will be equipped with a tether of 300 m kept at a negative voltage $|V| = 1$ kV with an estimated power consumption smaller than 3 W. The Coulomb drag generated by the tether should decrease the spacecraft altitude from 700 km to 500 km in half a year. A further planned mission that could serve as technological demonstrator of the plasma brake technology is FORESAIL-1, the first satellite designed by the Finnish centre Of excellence in REsearch of SustAInabLe space (FORESAIL) [165]. The 3U-CubeSat FORESAIL-1 should be launched in a polar orbit at an altitude of 700 km. The satellite will be equipped with scientific payloads to provide some *in-situ* measurements required for understanding the radiation belt physics and it will carry onboard a tether of 40 m for end-of-life deorbiting purposes [44]. Currently, the launch dates of ESTCube-2 and FORESAIL-1 are scheduled for 2022. If their outcomes will be positive, the plasma brake technology could be exploited in a near future for fast deorbiting of small satellites from LEOs. The recent interest in plasma brake technology and, in general, in Coulomb drag devices is also demonstrated by the private satellite AuroraSat-1, which is to be launched in June 2022 (see `https://aurorapt.fi/aurorasat-1/` for more details). AuroraSat-1 is a 1.5U-CubeSat equipped with two payloads, one of which is a plasma brake device that should enable a deorbiting from LEO.

The simplicity of the plasma brake concept has also led to a modification of the planned E-sail projects for deep space missions. Currently, a possible scenario for a test mission of the E-sail-based propulsion in deep space is constituted by a fleet of nanosatellites equipped with a single positively charged tether. In this regard, Slavinskis et al. [33] proposed the Multi-Asteroid Touring mission concept for a mid-term future mission. A fleet of 50 satellites (3U or 4U CubeSats), each one equipped with a 20 km tether, should aim at flyby with 20–30 primary target asteroids, while visiting hundreds of secondary targets during the transfer trajectories.

8. Conclusions

An extensive and accurate review of the electric solar wind sail technology has been discussed, starting from the initial proposal in 2004 and ending with the recent in-orbit experimental test attempts. All of the technological aspects involved in the development of the electric sail technology have been covered with particular attention on the proposed configurations, the dynamical behaviour, the manufacturing process, and the deployment phase. The latter is still one of the most challenging issues to be addressed before envisaging a deep space mission driven by a large electric sail structure. The available tools for modelling the thrust and torque vectors generated by an electric sail have also been thoroughly reviewed. Moreover, several possible applications in heliocentric scenarios have been discussed in order to highlight the potentialities of such an advanced propulsive system.

A deorbiting technology based on the electric sail working principle, the plasma brake, has also been presented and extensively discussed. Such a technology is potentially able to permit fast and low-cost deorbiting of satellites from low Earth orbits, and is especially well suited for small or medium spacecraft. The simplicity of the plasma brake concept, which only requires a single or few charged tethers, has led to the first experimental tests of this technology. It will probably influence the next deep space mission

scenarios, which could be based on electric sails constituted of a small number of tethers to reduce the system complexity and solve the deployment problem.

Conflict of interest statement

The authors declared that they have no conflicts of interest to this work.

References

[1] J. L. Wright, Space Sailing, Gordon and Breach Science Publishers, 1992.

[2] C. R. McInnes, Solar Sailing: Technology, Dynamics and Mission Applications, Springer-Verlag, Berlin, Germany, 1999.

[3] B. Fu, E. Sperber, F. Eke, Solar sail technology - A state of the art review, Progress in Aerospace Sciences 86 (2016) 1–19, doi: 10.1016/j.paerosci.2016.07.001.

[4] H. Sawada, O. Mori, N. Okuizumi, Y. Shirasawa, Y. Miyazaki, M. Natori, S. Matunaga, H. Furuya, H. Sakamoto, Mission report on the solar power sail deployment demonstration of IKAROS, in: 52nd AIAA/ASME/ASCE/AHS/ASC Structures, Structural Dynamics and Materials Conference, Denver (CO), USA, 2011, paper AIAA 2011-1887.

[5] D. A. Spencer, B. Betts, J. M. Bellardo, A. Diaz, B. Plante, J. R. Mansell, The LightSail 2 solar sailing technology demonstration, Advances in Space Research 67 (9) (2021) 2878–2889, doi: 10.1016/j.asr.2020.06.029.

[6] R. M. Zubrin, D. G. Andrews, Magnetic sails and interplanetary travel, Journal of Spacecraft and Rockets 28 (2) (1991) 197–203, doi: 10.2514/3.26230.

[7] D. G. Andrews, R. M. Zubrin, Magnetic sails and interstellar travel, Journal of the British Interplanetary Society 43 (6) (1990) 265–272 .

[8] D. G. Andrews, R. M. Zubrin, Progress in magnetic sails, in: AIAA/ASME/SAE/ASEE 26th Joint Propulsion Conference, Orlando (FL), USA, 1990, paper AIAA 90-2367.

[9] R. M. Zubrin, The use of magnetic sails to escape from low Earth orbit, Journal of the British Interplanetary Society 46 (3) (1992) 3–10, doi: 10.2514/6.1991-3352.

[10] N. Omidi, H. Karimabadi, Electrostatic Plasma Sail (EPS), in: 39th AIAA/ASME/SAE/ASEE Joint Propulsion Conference and Exhibit, Huntsville (AL), USA, 2003, paper AIAA 2003-5227.

[11] K. Fujita, Particle simulation of moderately-sized magnetic sails, The Journal of Space Technology and Science 20 (2) (2004) 26–31, doi: 10.11230/jsts.20.2_26.

[12] H. Nishida, H. Ogawa, I. Funaki, K. Fujita, H. Yamakawa, Y. Nakayama, Two-dimensional magnetohydrodynamic simulation of a magnetic sail, Journal of Spacecraft and Rockets 43 (3) (2006) 667–672, doi: 10.2514/1.15717.

[13] A. A. Quarta, G. Mengali, G. Aliasi, Optimal control laws for heliocentric transfers with a magnetic sail, Acta Astronautica 89 (2013) 216–225, doi: 10.1016/j.actaastro.2013.04.018.

[14] Y. Murayama, K. Ueno, Y. Oshio, H. Horisawa, I. Funaki, Preliminary results of magnetic field measurements on multi-coil magnetic sail in laboratory experiment, Vacuum 167 (2019) 509–513, doi: 10.1016/j.vacuum.2018.05.004.

[15] M. Bassetto, A. A. Quarta, G. Mengali, Magnetic sail-based displaced non-Keplerian orbits, Aerospace Science and Technology 92 (2019) 363–372, doi: 10.1016/j.ast.2019.06.018.

[16] M. Bassetto, A. A. Quarta, G. Mengali, Generalized sail trajectory approximation with applications to MagSails, Aerospace Science and Technology 118 (2021) Article number 106991, doi: 10.1016/j.ast.2021.106991.

[17] B. E. Gilchrist, L. Johnson, S. G. Bilén, Electrodynamic tethers as propulsion systems: system considerations and future plans, in: 35th Joint Propulsion Conference and Exhibit, AIAA, Los Angeles (CA), USA, 1999.

[18] J. R. Sanmartin, A review of electrodynamic tethers for science applications, Plasma Sources Science and Technology 19 (3) (2010) 1–7, doi: 10.1088/0963-0252/19/3/034022.

[19] P. Janhunen, Electric sail for spacecraft propulsion, Journal of Propulsion and Power 20 (4) (2004) 763–764, doi: 10.2514/1.8580.

[20] H. Djojodihardjo, R. I. Ahmed, A. Yousefian, Generic study of solar radiation and solar wind sailing, in: IEEE International Conference on Aerospace Electronics and Remote Sensing Technology (ICARES), Yogyakarta, Indonesia, 2014, pp. 147–156.

[21] H. Djojodihardjo, Overview and analysis of MSAIL and ESAIL propulsion for interplanetary missions, in: Proceedings of the 68th International Astronautical Congress (IAC), Vol. 14, Adelaide, Australia, 2017, pp. 8974–8991.

[22] P. Janhunen, Electric solar wind sail in-space propulsion status report, in: European Planetary Science Congress, Vol. 5, European Planetology Network and the European Geosciences Union, San Sebastian, Spain, 2010, paper EPSC 2010-297.

[23] P. Janhunen, Status report of the electric sail in 2009, Acta Astronautica 68 (5-6) (2011) 567–570, doi: 10.1016/j.actaastro.2010.02.007.

[24] L. Johnson, M. Meyer, B. Palaszewski, D. Coote, D. Goebel, H. White, Development priorities for in-space propulsion technologies, Acta Astronautica 82 (2) (2013) 148–152, doi: 10.1016/j.actaastro.2012.05.006.

[25] P. K. Toivanen, P. Janhunen, Spin plane control and thrust vectoring of electric solar wind sail, Journal of Propulsion and Power 29 (1) (2013) 178–185, doi: 10.2514/1.B34330.

[26] P. K. Toivanen, P. Janhunen, Electric solar wind sail: Deployment, long-term dynamics, and control hardware requirements, in: M. Macdonald (Ed.), Advances in Solar Sailing, Springer Praxis, Chichester, UK, 2014, pp. 977–987.

[27] P. Janhunen, P. K. Toivanen, TI tether ring for solving secular spinrate change problem of electric sail, arXiv:1603.05563 (2017).

[28] P. Janhunen, A. A. Quarta, G. Mengali, Electric solar wind sail mass budget model, Geoscientific Instrumentation, Methods and Data Systems 2 (1) (2013) 85–95, doi: 10.5194/gi-2-85-2013.

[29] P. Janhunen, P. K. Toivanen, An intrinsic way to control E-sail spin, arXiv:1406.6847 (2014).

[30] J. Kang, K.-C. Park, Flexible heliogyro solar sail under solar radiation pressure and gravitational force, Acta Astronautica 179 (2021) 186–196, doi: 10.1016/j.actaastro.2020.10.042.
[31] P. Janhunen, Photonic spin control for solar wind electric sail, Acta Astronautica 83 (2013) 85–90, doi: 10.1016/j.actaastro.2012.10.017.
[32] P. Janhunen, Electric sail, photonic sail and deorbiting applications of the freely guided photonic blade, Acta Astronautica 93 (2014) 410–417, doi: 10.1016/j.actaastro.2013.07.041.
[33] A. Slavinskis, P. Janhunen, P. Toivanen, K. Muinonen, A. Penttilä, M. Granvik, T. Kohout, M. Gritsevich, M. Pajusalu, I. Sunter, H. Ehrpais, J. Dalbins, I. Iakubivskyi, T. Eenmäe, E. Ilbis, D. Mauro, J. Stupl, A. S. Rivkin, W. F. Bottke, Nanospacecraft fleet for multi-asteroid touring with electric solar wind sails, in: IEEE Aerospace Conference Proceedings, Vol. 2018-March, Big Sky (MT), USA, 2018, pp. 1–20.
[34] J. Fulton, H. Schaub, Dynamics and control of the flexible electrostatic sail deployment, in: 26th AAS/AIAA Space Flight Mechanics Meeting, Napa (CA), USA, 2016, paper AAS-16-499.
[35] J. Fulton, H. Schaub, Fixed-axis electric sail deployment dynamics analysis using hub-mounted momentum control, Acta Astronautica 144 (2018) 160–170, doi: 10.1016/j.actaastro.2017.11.048.
[36] G. Li, Z. H. Zhu, C. Du, Stability and control of radial deployment of electric solar wind sail, Nonlinear Dynamics 103 (1) (2021) 481–501, doi: 10.1007/s11071-020-06067-7.
[37] R. Rosta, O. Krömer, T. Zoest, P. Janhunen, M. Noorma, Wrecker: an unreeling mechanism for a thin electrically conductive space tether, CEAS Space Journal 7 (1) (2018) 53–68, doi: 10.1007/s12567-015-0080-6.
[38] O. Krömer, R. Rosta, L. Richter, P. Janhunen, SAMUEL - Space Applied Mechanism for Unreeling Electric conductive tethers, in: European Planetary Science Congress, Rome, Italy, 2010, paper EPSC 2010-229.
[39] O. Khurshid, T. Tikka, J. Praks, M. Hallikainen, Accomodating the plasma brake experiment on-board the Aalto-1 satellite, Proceedings of the Estonian Academy of Sciences 63 (2S) (2014) 258–266, doi: 10.3176/proc.2014.2S.07.
[40] R. L. Forward, R. P. Hoyt, Failsafe multiline Hoytether lifetimes, in: 31st Joint Propulsion Conference and Exhibit, San Diego (CA), USA, 1995, paper AIAA-95-2890.
[41] R. L. Forward, R. P. Hoyt, C. W. Uphoff, Terminator Tether: A spacecraft deorbit device, Journal of Spacecraft and Rockets 37 (2) (2000) 187–196, doi: 10.2514/2.3565.
[42] H. Seppänen, T. Rauhala, S. Kiprich, J. Ukkonen, M. Simonsson, R. Kurppa, P. Janhunen, E. Hæggström, One kilometer (1 km) electric solar wind sail tether produced automatically, Review of Scientific Instruments 84 (9) (2013) 095102–1–095102–14, doi: 10.1063/1.4819795.
[43] T. Rauhala, H. Seppänen, J. Ukkonen, S. Kiprich, G. Maconi, P. Janhunen, E. Hæggström, Automatic 4-wire Heytether production for the electric solar wind sail, in: International Microelectronics Assembly and Packing Society Topical Workshop and Tabletop Exhibition on Wire Bonding, San Jose (CA), USA, 2013.
[44] I. Iakubivskyi, P. Janhunen, J. Praks, V. Allik, K. Bussov, B. Clayhills, J. Dalbins, T. Eenmäe, H. Ehrpais, J. Envall, S. Haslam, E. Ilbis, N. Jovanovic, E. Kilpua, J. Kivastik, J. Laks, P. Laufer, M. Merisalu, M. Meskanen, R. Märk, A. Nath, P. Niemelä, M. Noorma, M. R. Mughal, S. Nyman, M. Pajusalu, M. Palmroth, A. S. Paul, T. Peltola, M. Plans, J. Polkko, Q. S. Islam, A. Reinart, B. Riwanto, V. Sammelselg, J. Sate, I. Sünter, M. Tajmar, E. Tanskanen, H. Teras, P. Toivanen, R. Vainio, M. Väänänen, A. Slavinskis, Coulomb drag propulsion experiments of ESTCube-2 and FORESAIL-1, Acta Astronautica 177 (2020) 771–783, doi: 10.1016/j.actaastro.2019.11.030.
[45] P. K. Toivanen, P. Janhunen, Thrust vectoring of an electric solar wind sail with a realistic sail shape, Acta Astronautica 131 (2017) 145–151, doi: 10.1016/j.actaastro.2016.11.027.
[46] M. Bassetto, G. Mengali, A. A. Quarta, Thrust and torque vector characteristics of axially-symmetric E-sail, Acta Astronautica 146 (2018) 134–143, doi: 10.1016/j.actaastro.2018.02.035.
[47] F. Liu, Q. Hu, Y. Liu, Attitude dynamics of electric sail from multibody perspective, Journal of Guidance, Control, and Dynamics 41 (12) (2018) 2633–2646, doi: 10.2514/1.G003625.
[48] R. Wang, C. Wei, Y. Wu, Y. Zhao, The study of spin control of flexible electric sail using the absolute nodal coordinate formulation, in: IEEE International Conference on Cybernetics and Intelligent Systems, CIS 2017 and IEEE Conference on Robotics, Automation and Mechatronics, RAM, Vol. 2018-January, Ningbo, China, 2018, pp. 785–790.
[49] G. Li, Z. H. Zhu, C. Du, S. A. Meguid, Characteristics of coupled orbital-attitude dynamics of flexible electric solar wind sail, Acta Astronautica 159 (2019) 593–608, doi: 10.1016/j.actaastro.2019.02.009.
[50] C. Zhao, M.-Y. Huo, J. Qi, S. Cao, D. Zhu, L. Sun, H. Sun, N. Qi, Coupled attitude-vibration analysis of an E-sail using absolute nodal coordinate formulation, Astrodynamics 4 (3) (2020) 249–263, doi: 10.1007/s42064-020-0081-x.
[51] H. Ren, K. Yang, A referenced nodal coordinate formulation, Multibody System Dynamics 51 (3) (2021) 305–342, doi: 10.1007/s11044-020-09750-0.
[52] L. Boni, M. Bassetto, G. Mengali, A. A. Quarta, Electric sail static structural analysis with finite element approach, Acta Astronautica 175 (2020) 510–516, doi: 10.1016/j.actaastro.2020.06.009.
[53] T. D. Lillian, Modal analysis of electric sail, Acta Astronautica 185 (2021) 140–147, doi: 10.1016/j.actaastro.2021.05.003.
[54] P. Janhunen, P. K. Toivanen, Safety criteria for flying E-sail through solar eclipse, Acta Astronautica 114 (2015) 1–5, doi: 10.1016/j.actaastro.2015.04.006.
[55] P. Janhunen, A. Sandroos, Simulation study of solar wind push on a charged wire: basis of solar wind electric sail propulsion, Annales Geophysicae 25 (3) (2007) 755–767, doi: 10.5194/angeo-25-755-2007.
[56] G. Mengali, A. A. Quarta, P. Janhunen, Electric sail performance analysis, Journal of Spacecraft and Rockets 45 (1) (2008) 122–129, doi: 10.2514/1.31769.
[57] P. Janhunen, Electrostatic plasma brake for deorbiting a satellite, Journal of Propulsion and Power 26 (2) (2010) 370–372, doi: 10.2514/1.47537.
[58] P. Janhunen, Increased electric sail thrust through removal of trapped shielding electrons by orbit chaotisation due to spacecraft body, Annales Geophysicae 27 (8) (2009) 3089–3100, doi: 10.5194/angeo-27-3089-2009.
[59] P. Janhunen, P. K. Toivanen, J. Polkko, S. Merikallio, P. Salminen, E. Haeggström, H. Seppänen, R. Kurppa, J. Ukkonen, S. Kiprich, G. Thornell, H. Kratz, L. Richter, O. Krömer, R. Rosta, M. Noorma, J. Envall, S. Lätt, G. Mengali, A. A.

Quarta, H. Koivisto, O. Tarvainen, T. Kalvas, J. Kauppinen, A. Nuottajärvi, A. Obraztsov, Electric solar wind sail: toward test missions, Review of Scientific Instruments 81 (11) (2010) 111301–1–11301–11, doi: 10.1063/1.3514548.
[60] K. Yamaguchi, H. Yamakawa, Study on orbital maneuvers for electric sail with on-off thrust control, Aerospace Technology Japan, the Japan Society for Aeronautical and Space Sciences 12 (2013) 79–88, doi: 10.2322/astj.12.79.
[61] M.-Y. Huo, G. Mengali, A. A. Quarta, Electric sail thrust model from a geometrical perspective, Journal of Guidance, Control, and Dynamics 41 (3) (2018) 735–741, doi: 10.2514/1.G003169.
[62] A. A. Quarta, G. Mengali, Minimum-time trajectories of electric sail with advanced thrust model, Aerospace Science and Technology 55 (2016) 419–430, doi: 10.1016/j.ast.2016.06.020.
[63] K. Yamaguchi, K. Miyata, Orbital maneuvering of electric solar wind sail based on an advanced solar wind force model, Acta Astronautica 166 (2020) 417–430, doi: 10.1016/j.actaastro.2019.10.001.
[64] C. Du, Z. H. Zhu, G. Li, Analysis of thrust-induced sail plane coning and attitude motion of electric sail, Acta Astronautica 178 (2021) 129–142, doi: 10.1016/j.actaastro.2020.09.001.
[65] M. Bassetto, G. Mengali, A. A. Quarta, Stability and control of spinning E-sail in heliostationary orbit, Journal of Guidance, Control, and Dynamics 42 (2) (2019) 425–431, doi: 10.2514/1.G003788.
[66] M. J. H. Walker, B. Ireland, J. Owens, A set of modified equinoctial orbit elements, Celestial Mechanics 36 (4) (1985) 409–419, doi: 10.1007/BF01227493.
[67] M. J. H. Walker, Erratum: a set of modified equinoctial orbit elements, Celestial Mechanics 38 (4) (1986) 391–392, doi: 10.1007/BF01238929.
[68] J. T. Betts, Very low-thrust trajectory optimization using a direct SQP method, Journal of Computational and Applied Mathematics 120 (1) (2000) 27–40, doi: 10.1016/S0377-0427(00)00301-0.
[69] L. Niccolai, A. A. Quarta, G. Mengali, Two-dimensional heliocentric dynamics approximation of an electric sail with fixed attitude, Aerospace Science and Technology 71 (2017) 441–446, doi: 10.1016/j.ast.2017.09.045.
[70] M.-Y. Huo, G. Mengali, A. A. Quarta, Accurate approximation of in-ecliptic trajectories for E-sail with constant pitch angle, Advances in Space Research 61 (10) (2018) 2617–2627, doi: 10.1016/j.asr.2018.02.034.
[71] M.-Y. Huo, G. Mengali, A. A. Quarta, N. Qi, Electric sail trajectory design with Bezier curve-based shaping approach, Aerospace Science and Technology 88 (2019) 126–135, doi: 10.1016/j.ast.2019.03.023.
[72] G. Aliasi, G. Mengali, A. A. Quarta, Artificial equilibrium points for an electric sail with constant attitude, Journal of Spacecraft and Rockets 50 (6) (2013) 1295–1298, doi: 10.2514/1.A32540.
[73] J. R. Wertz (Ed.), Spacecraft attitude determination and control, 1st Edition, Astrophysics and Space Science Library, Springer Netherlands, Dordrecht, Netherlands, 1978, pp. 760–766, doi: 10.1007/978-94-009-9907-7.
[74] A. A. Quarta, G. Mengali, P. Janhunen, Optimal interplanetary rendezvous combining electric sail and high thrust propulsion system, Acta Astronautica 68 (5-6) (2011) 603–621, doi: 10.1016/j.actaastro.2010.01.024.
[75] G. Mengali, A. A. Quarta, Optimal nodal flyby with near-Earth asteroids using electric sail, Acta Astronautica 104 (2) (2014) 450–457, doi: 10.1016/j.actaastro.2014.02.012.
[76] A. A. Quarta, G. Aliasi, G. Mengali, Electric solar wind sail optimal transit in the circular restricted three body problem, Acta Astronautica 116 (2015) 43–49, doi: 10.1016/j.actaastro.2015.06.017.
[77] A. A. Quarta, G. Mengali, P. Janhunen, Electric sail option for cometary rendezvous, Acta Astronautica 127 (2016) 684–692, doi: 10.1016/j.actaastro.2016.06.020.
[78] M.-Y. Huo, G. Mengali, A. A. Quarta, Optimal planetary rendezvous with an electric sail, Aircraft Engineering and Aerospace Technology 88 (4) (2016) 515–522, doi: 10.1108/AEAT-01-2015-0012.
[79] D. F. Lawden, Optimal Trajectories for Space Navigation, Butterworths & Co., London, UK, 1963, pp. 54–60.
[80] Y. Wang, Y. Wei, Y. Li, Y. Yu, B. Bian, Trajectory optimization of electric sail based on particle swarm algorithm, Zhongguo Kongjian Kexue Jishu/Chinese Space Science and Technology 35 (3) (2015) 26–34, doi: 10.3780/j.issn.1000-758X.2015.03.004.
[81] N.-M. Qi, M.-Y. Huo, Q.-F. Yuan, Electric sail trajectory optimization and performance analysis, Yuhang Xuebao/Journal of Astronautics 34 (5) (2013) 634–641, doi: 10.3873/j.issn.1000-1328.2013.05.006.
[82] M.-Y. Huo, N. Qi, T. Wang, Hybrid genetic algorithm Gauss pseudospectral method for the electric sail trajectory optimization, in: 2nd International Conference on Instrumentation and Measurement, Computer, Communication and Control (IMCCC), Hangzhou, China, 2012, pp. 318–322.
[83] M.-Y. Huo, F.-J. Peng, J. Zhao, S.-B. Xie, N.-M. Qi, Trajectory optimization for Ceres exploration with an electric sail, Yuhang Xuebao/Journal of Astronautics 36 (12) (2015) 1363–1372, doi: 10.3873/j.issn.1000-1328.2015.12.004.
[84] M. Bassetto, A. A. Quarta, G. Mengali, Locally-optimal electric sail transfer, Proceedings of the Institution of Mechanical Engineers, Part G: Journal of Aerospace Engineering 233 (1) (2019) 166–179, doi: 10.1177/0954410017728975.
[85] M. Bassetto, A. A. Quarta, G. Mengali, V. Cipolla, Spiral trajectories induced by radial thrust with applications to generalized sails, Astrodynamics 5 (2) (2020) 121–137, doi: 10.1007/s42064-020-0093-6.
[86] L. Niccolai, A. A. Quarta, G. Mengali, Electric sail-based displaced orbits with refined thrust model, Proceedings of the Institution of Mechanical Engineers, Part G: Journal of Aerospace Engineering 232 (3) (2018) 423–432, doi: 10.1177/0954410016679195.
[87] M. Bassetto, G. Mengali, A. A. Quarta, Attitude dynamics of an electric sail model with a realistic shape, Acta Astronautica 159 (2019) 250–257, doi: 10.1016/j.actaastro.2019.03.064.
[88] M. Bassetto, G. Mengali, A. A. Quarta, E-sail attitude control with tether voltage modulation, Acta Astronautica 166 (2020) 350–357, doi: 10.1016/j.actaastro.2019.10.023.
[89] G. Li, Z. H. Zhu, C. Du, Flight dynamics and control strategy of electric solar wind sails, Journal of Guidance, Control, and Dynamics 43 (3) (2020) 462–474, doi: 10.2514/1.G004608.
[90] L. Huang, H. Wen, L. Cheng, S. Xu, Nonlinear model predictive control for attitude maneuver of a barbell electric sail through voltage regulation, Acta Astronautica 179 (2021) 146–152, doi: 10.1016/j.actaastro.2020.10.028.
[91] C. Du, Z. H. Zhu, G. Li, Rigid-flexible coupling effect on attitude dynamics of electric solar wind sail, Communications in Nonlinear Science and Numerical Simulation 95 (2021) Article number 105663, doi: 10.1016/j.cnsns.2020.105663.

[92] P. Janhunen, The electric sail - A new propulsion method which may enable fast missions to the outer solar system, JBIS - Journal of the British Interplanetary Society 61 (8) (2008) 322–325 .
[93] M. Bassetto, in V. Badescu, K. Zacny, and Y. Bar-Cohen Springer Handbook of Space Resources, Springer, in press, Ch. *"Tracking and thrust vectoring of E-sail-based spacecraft for solar activity monitoring"*.
[94] G. Mengali, A. A. Quarta, P. Janhunen, Considerations of electric sailcraft trajectory design, Journal of the British Interplanetary Society 61 (8) (2008) 326–329 .
[95] P. Janhunen, J.-P. Lebreton, S. Merikallio, M. Paton, G. Mengali, A. A. Quarta, Fast E-sail Uranus entry probe mission, Planetary and Space Science 104 (2014) 141–146, doi: 10.1016/j.pss.2014.08.004.
[96] A. A. Quarta, G. Mengali, Electric sail mission analysis for outer solar system exploration, Journal of Guidance, Control, and Dynamics 33 (3) (2010) 740–755, doi: 10.2514/1.47006.
[97] M. Leipold, O. Wagner, 'Solar photonic assist' trajectory design for solar sail missions to the outer solar system and beyond, in: AAS/GSFC International Symposium on Flight Dynamics, Greenbelt (MD), USA, 1998, Paper AAS 98-386.
[98] M.-Y. Huo, G. Mengali, A. A. Quarta, Mission design for an interstellar probe with E-sail propulsion system, JBIS - Journal of the British Interplanetary Society 68 (5-6) (2015) 128–134 .
[99] G. Aliasi, G. Mengali, A. A. Quarta, Artificial equilibrium points for a generalized sail in the circular restricted three-body problem, Celestial Mechanics and Dynamical Astronomy 110 (4) (2011) 343–368, doi: 10.1007/s10569-011-9366-y.
[100] G. Aliasi, G. Mengali, A. A. Quarta, Artificial equilibrium points for a generalized sail in the elliptic restricted three-body problem, Celestial Mechanics and Dynamical Astronomy 114 (1–2) (2012) 181–200, doi: 10.1007/s10569-012-9425-z.
[101] L. Niccolai, A. Caruso, A. A. Quarta, G. Mengali, Artificial collinear Lagrangian point maintenance with electric solar wind sail, IEEE Transactions on Aerospace and Electronic Systems 56 (6) (2020) 4467–4477, doi: 10.1109/TAES.2020.2990805.
[102] W. Wang, G. Mengali, A. A. Quarta, H. Baoyin, Decentralized fault-tolerant control for multiple electric sail relative motion at artificial Lagrange points, Aerospace Science and Technology 103 (2020) Article number 105904, doi: 10.1016/j.ast.2020.105904.
[103] A. A. Quarta, G. Mengali, Electric sail missions to potentially hazardous asteroids, Acta Astronautica 66 (9-10) (2010) 1506–1519, doi: 10.1016/j.actaastro.2009.11.021.
[104] L. Niccolai, A. A. Quarta, G. Mengali, in V. Badescu, K. Zacny, and Y. Bar-Cohen Springer Handbook of Space Resources, Springer, in press, Ch. *"Exploration of asteroids and cometswith innovative propulsion systems"*.
[105] A. A. Quarta, G. Mengali, P. Janhunen, Electric sail for a near-Earth asteroid sample return mission: case 1998 KY26, Journal of Aerospace Engineering 27 (6) (2014) Article number 4014031, doi: 10.1061/(ASCE)AS.1943-5525.0000285.
[106] K. Yamaguchi, H. Yamakawa, Electric solar wind sail kinetic energy impactor for Near Earth Asteroid deflection mission, The Journal of the Astronautical Sciences 63 (1) (2016) 1–22, doi: 10.1007/s40295-015-0081-x.
[107] G. Mengali, A. A. Quarta, Non-Keplerian orbits for electric sails, Celestial Mechanics and Dynamical Astronomy 105 (1–3) (2009) 179–195, doi: 10.1007/s10569-009-9200-y.
[108] L. Niccolai, A. A. Quarta, G. Mengali, in V. Badescu, K. Zacny, and Y. Bar-Cohen Springer Handbook of Space Resources, Springer, in press, Ch. *"Displaced non-Keplerian orbits for Sunand inner planet observation"*.
[109] L. Niccolai, A. A. Quarta, G. Mengali, Electric sail elliptic displaced orbits with advanced thrust model, Acta Astronautica 138 (2017) 503–511, doi: 10.1016/j.actaastro.2016.10.036.
[110] X. Pan, A. A. Quarta, G. Mengali, M. Xu, Linearized relative motion and proximity control of E-sail-based displaced orbits, Aerospace Science and Technology 99 (2020) Article number 105574, doi: 10.1016/j.ast.2019.105574.
[111] W. Wang, G. Mengali, A. A. Quarta, J. Yuan, Formation flying for electric sails in displaced orbits. Part I: geometrical analysis, Advances in Space Research 60 (6) (2017) 1115–1129, doi: 10.1016/j.asr.2017.05.015.
[112] W. Wang, G. Mengali, A. A. Quarta, J. Yuan, Formation flying for electric sails in displaced orbits. Part II: distributed coordinated control, Advances in Space Research 60 (6) (2017) 1130–1147, doi: 10.1016/j.asr.2017.06.017.
[113] G. Mengali, A. A. Quarta, G. Aliasi, Heliocentric phasing performance of electric sail spacecraft, Acta Astronautica 127 (2016) 474–481, doi: 10.1016/j.actaastro.2016.06.033.
[114] L. Niccolai, A. Caruso, A. A. Quarta, G. Mengali, Electric sail phasing maneuvers for constellation deployment, Acta Astronautica 177 (2020) 853–861, doi: 10.1016/j.actaastro.2019.12.003.
[115] M. Bassetto, L. Boni, G. Mengali, A. A. Quarta, Electric sail phasing maneuvers with radial thrust, Acta Astronautica 179 (2021) 99–104, doi: 10.1016/j.actaastro.2020.10.025.
[116] G. Mengali, A. A. Quarta, G. Aliasi, A graphical approach to electric sail mission design with radial thrust, Acta Astronautica 82 (2) (2013) 197–208, doi: 10.1016/j.actaastro.2012.03.022.
[117] A. A. Quarta, G. Mengali, Analysis of electric sail heliocentric motion under radial thrust, Journal of Guidance, Control, and Dynamics 39 (6) (2016) 1431–1435, doi: 10.2514/1.G001632.
[118] P. Janhunen, S. Merikallio, M. Paton, EMMI - Electric solar wind sail facilitated Manned Mars Initiative, Acta Astronautica 113 (2015) 22–28, doi: 10.1016/j.actaastro.2015.03.029.
[119] M. Lingam, A. Loeb, Electric sails are potentially more effective than light sails near most stars, Acta Astronautica 168 (2020) 146–154, doi: 10.1016/j.actaastro.2019.12.013.
[120] N. Perakis, A. M. Hein, Combining magnetic and electric sails for interstellar deceleration, Acta Astronautica 128 (2016) 13–20, doi: 10.1016/j.actaastro.2016.07.005.
[121] L. Gallana, F. Fraternale, S. M. Fosson, E. Magli, M. Opher, J. D. Richardson, D. Tordella, Voyager 2 solar plasma and magnetic field spectral analysis for intermediate data sparsity, Journal of Geophysical Research A: Space Physics 121 (5) (2016) 3905–3919, doi: 10.1002/2015JA021830.
[122] J. L. Phillips, S. J. Bame, A. Barnes, B. M. Barraclough, W. C. Feldman, B. E. Goldstein, Ulysses solar wind plasma observations from pole to pole, Geophysical Research Letters 22 (23) (1995) 3301–3304, doi: 10.1029/95GL03094.
[123] E. C. Stone, A. M. Frandsen, R. A. Mewaldt, E. R. Christian, D. Margolies, J. F. Ormes, The Advanced Composition Explorer, Space Science Reviews 86 (1–4) (1998) 1–22, doi: 10.1007/978-94-011-4762-0_1.
[124] P. K. Toivanen, P. Janhunen, Electric sailing under observed solar wind conditions, Astrophysics and Space Science

Transactions 5 (1) (2009) 61–69, doi: 10.5194/astra-5-61-2009.
[125] Y. Wang, B. Bian, Trajectory tracking control of electric sail with input uncertainty and saturation constraint, Transactions of the Institute of Measurement and Control 39 (7) (2017) 1007–1016, doi: 10.1177/0142331215625771.
[126] L. Niccolai, A. Anderlini, G. Mengali, A. A. Quarta, Impact of solar wind fluctuations on electric sail mission design, Aerospace Science and Technology 82-83 (2018) 38–45, doi: 10.1016/j.ast.2018.08.032.
[127] L. Niccolai, A. Anderlini, G. Mengali, A. A. Quarta, Electric sail displaced orbit control with solar wind uncertainties, Acta Astronautica 162 (2019) 563–573, doi: 10.1016/j.actaastro.2019.06.037.
[128] D. Xiu, G. E. Karniadakis, The Wiener-Askey polynomial chaos for stochastic differential equations, SIAM Journal on Scientific Computing 24 (2) (2003) 619–644, doi: 10.1137/S1064827501387826.
[129] A. Caruso, L. Niccolai, G. Mengali, A. A. Quarta, Electric sail trajectory correction in presence of environmental uncertainties, Aerospace Science and Technology 94 (2019) Article number 105395, doi: 10.1016/j.ast.2019.105395.
[130] B. Bastida Virgili, H. Krag, Strategies for active removal in LEO, in: 5th European Conference on Space Debris, European Space Agency (ESA), Darmstadt, Germany, 2009.
[131] P. Janhunen, On the feasibility of a negative polarity electric sail, Annales Geophysicae 27 (4) (2009) 1439–1447, doi: 10.5194/angeo-27-1439-2009.
[132] L. Orsini, L. Niccolai, G. Mengali, A. A. Quarta, Plasma brake model for preliminary mission analysis, Acta Astronautica 144 (2017) 297–304, doi: 10.1016/j.actaastro.2017.12.048.
[133] F. Schäfer, M. Lambert, E. Christiansen, S. Kibe, H. Stokes, H. G. Reimerdes, S. A. Meshcheryakov, F. Angrilli, H. Zengyao, The Inter-Agency Space Debris Coordination Committee (IADC) protection manual, in: 4th European Conference on Space Debris, European Space Agency (ESA), Darmstadt, Germany, 2005.
[134] M. Yakovlev, The "IADC space debris mitigation guidelines" and support document, in: 4th European Conference on Space Debris, European Space Agency (ESA), Darmstadt, Germany, 2005.
[135] J. E. Allen, Probe theory - The orbital motion approach, Physica Scripta 45 (5) (1992) 497–503, doi: 10.1088/0031-8949/45/5/013.
[136] P. Janhunen, Simulation study of the plasma-brake effect, Annales Geophysicae 32 (2014) 1207–1216, doi: 10.5194/angeo-32-1207-2014.
[137] K. Rawer, D. Bilitza, S. Ramakrishnan, Goals and status of the International Reference Ionosphere, Reviews of Geophysics 16 (2) (1978) 177–181, doi: 10.1029/RG016i002p00177.
[138] D. Bilitza, K. Rawer, L. Bossy, T. Gulyaeva, International Reference Ionosphere – past, present, and future: I. Electron density, Advances in Space Research 13 (3) (1993) 3–13, doi: 10.1016/0273-1177(93)90240-C.
[139] D. Bilitza, K. Rawer, L. Bossy, T. Gulyaeva, International Reference Ionosphere – past, present, and future: II. Plasma temperatures, ion composition and ion drift, Advances in Space Research 13 (3) (1993) 15–23, doi: 10.1016/0273-1177(93)90241-3.
[140] D. Bilitza, International Reference Ionosphere 2000: examples of improvements and new features, Advances in Space Research 31 (3) (2003) 757–767, doi: 10.1016/S0273-1177(03)00020-6.
[141] D. Bilitza, B. W. Reinisch, S. M. Radicella, S. Pulinets, T. Gulyaeva, L. Triskova, Improvements of the International Reference Ionosphere model for the topside electron density profile, Radio Science 41 (5) (2006) 1–8, doi: 10.1029/2005RS003370.
[142] D. Bilitza, B. W. Reinisch, International Reference Ionosphere 2007: improvements and new parameters, Advances in Space Research 42 (4) (2008) 599–609, doi: 10.1016/j.asr.2007.07.048.
[143] D. Bilitza, The International Reference Ionosphere - Status 2013, Advances in Space Research 55 (8) (2015) 1914–1927, doi: 10.1016/j.asr.2014.07.032.
[144] A. E. Hedin, J. E. Salah, J. V. Evans, et al., A global thermospheric model based on mass spectrometer and incoherent scatter data 1. N_2 density and temperature, Journal of Geophysical Research 82 (16) (1977) 2139–2147, doi: 10.1029/JA082i016p02139.
[145] A. E. Hedin, C. A. Reber, G. P. Newton, N. W. Spencer, H. C. Brinton, H. G. Mayr, W. E. Potter, A global thermospheric model based on mass spectrometer and incoherent scatter data 2. Composition, Journal of Geophysical Research 82 (16) (1977) 2148–2156, doi: 10.1029/JA082i016p02148.
[146] L. Niccolai, M. Bassetto, A. A. Quarta, G. Mengali, Plasma brake approximate trajectory. Part I: geocentric motion, in: 4th IAA Conference on University Satellite Missions and CubeSat Workshop, IAA, Rome, Italy, 2017.
[147] M. Bassetto, L. Niccolai, A. A. Quarta, G. Mengali, Plasma brake approximate trajectory. Part II: relative motion, in: 4th IAA Conference on University Satellite Missions and CubeSat Workshop, IAA, Rome, Italy, 2017.
[148] W. H. Clohessy, W. R. S., Terminal guidance system for satellite rendezvous, Journal of the Aerospace Sciences 27 (9) (1960) 653–658, doi: 10.2514/8.8704.
[149] P. Janhunen, Coulomb drag devices: electric solar wind sail propulsion and ionospheric deorbiting, in: Space propulsion 2014, Köln, Germany, 2014.
[150] P. Janhunen, P. K. Toivanen, J. Envall, A. Slavinskis, Using charges tether Coulomb drag: E-sail and plasma brake, in: 5th International Conference on Tethers in Space, Ann Arbor (MI), USA, 2016.
[151] C. K. Birdsall, A. B. Langdon, Plasma physics via computer simulation, Adam Hilger, New York (NY), USA, 1991.
[152] U. Kvell, D. Di Cara, P. Janhunen, M. Noorma, J. A. Gonzalez del Amo, Deorbiting strategies: comparison between electrostatic plasma brake and conventional propulsion, in: 47th AIAA/ASME/SAE/ASEE Joint Propulsion Conference & Exhibit, San Diego (CA), USA, 2011, paper AIAA 2011-5920.
[153] C. Ham, D. Ngo, Deorbiting of LEO small satellites without a conventional propulsion system, in: IEEE SoutheastCon, Charlotte (NC), USA, 2017, pp. 1–2.
[154] J. R. Sanmartin, E. Choiniere, B. E. Gilchrist, J. B. Ferry, M. Martinez-Sanchez, Bare-tether sheath and current: comparison of asymptotic theory and kinetic simulations in stationary plasma, IEEE Transactions on Plasma Science 36 (5) (2008) 2851–2858, doi: 10.1109/TPS.2008.2003978.
[155] R. Zhong, Z. H. Zhu, Dynamics of nanosatellite deorbit by bare electrodynamic tether in Low Earth Orbit, Journal of

Spacecraft and Rockets 50 (3) (2013) 691–700, doi: 10.2514/1.A32336.
[156] G. Sanchez-Arriaga, J. R. Sanmartin, E. C. Lorenzini, Comparison of technologies for deorbiting spacecraft from low-Earth-orbit at end of mission, Acta Astronautica 138 (2017) 536–542, doi: 10.1016/j.actaastro.2016.12.004.
[157] S. Lätt, A. Slavinskis, E. Ilbis, U. Kvell, K. Voormansik, E. Kulu, M. Pajusalu, H. Kuuste, I. Sünter, T. Eenmäe, K. Laizans, K. Zalite, R. Vendt, J. Piepenbrock, I. Ansko, A. Leitu, A. Vahter, A. Agu, E. Eilonen, E. Soolo, H. Ehrpais, H. Lillmaa, I. Mahhonin, J. Mõttus, J. Viru, J. Kalde, J. Subitidze, J. Mucenieks, J. Sate, J. Kütt, J. Polevskis, J. Laks, K. Kivistik, K.-L. Kusmin, K.-G. Kruus, K. Tarbe, K. Tuude, K. Kalnina, L. Joost, M. Lõoke, M. Järve, M. Vellak, M. Neerot, M. Valgur, M. Pelakauskas, M. Averin, M. Mikkor, M. Veske, O. Scheler, P. Liias, P. Laes, R. Rantsus, R. Soosaar, R. Reinumägi, R. Valner, S. Kurvits, S.-E. Mändmaa, T. Ilves, T. Peet, T. Ani, T. Tilk, T. H. C. Tamm, T. Scheffler, T. Vahter, T. Uiboupin, V. Evard, A. Sisask, L. Kimmel, O. Krömer, R. Rosta, P. Janhunen, J. Envall, P. K. Toivanen, T. Rauhala, H. Seppänen, J. Ukkonen, E. Haeggström, R. Kurppa, T. Kalvas, O. Tarvainen, J. Kauppinen, A. Nuottajärvi, H. Koivisto, S. Kiprich, A. Obraztsov, V. Allik, A. Reinart, M. Noorma, ESTCube-1 nanosatellite for electric solar wind sail in-orbit technology demonstration, Proceedings of the Estonian Academy of Sciences 63 (2S) (2014) 200–209, doi: 10.3176/proc.2014.2S.01.
[158] J. Envall, P. Janhunen, P. K. Toivanen, M. Pajusalu, E. Ilbis, J. Kalde, M. Averin, H. Kuuste, K. Laizans, V. Allik, T. Rauhala, H. Seppänen, S. Kiprich, J. Ukkonen, E. Haeggström, T. Kalvas, O. Tarvainen, J. Kauppinen, A. Nuottajärvi, H. Koivisto, E-sail test payload of the ESTCube-1 nanosatellite, Proceedings of the Estonian Academy of Sciences 63 (2S) (2014) 210–221, doi: 10.3176/proc.2014.2S.02.
[159] I. Iakubivskyi, H. Ehrpais, J. Dalbins, E. Oro, E. Kulu, J. Kütt, P. Janhunen, A. Slavinskis, E. Ilbis, I. Ploom, I. Sünter, R. Trops, M. Merisalu, K. Rejnkubjas, ESTCube-2 mission analysis: plasma brake experiment for deorbiting, in: Proceedings of the 67th International Astronautical Congress (IAC), Guadalajara, Mexico, 2016, paper IAC-16,E2,4,4,x33190.
[160] A. Slavinskis, M. Pajusalu, H. Kuuste, E. Ilbis, T. Eenmäe, I. Sünter, K. Laizans, H. Ehrpais, P. Liias, E. Kulu, J. Viru, J. Kalde, U. Kvell, U. Kütt, K. Zalite, K. Kahn, S. Lätt, J. Envall, P. K. Toivanen, J. Polkko, P. Janhunen, R. Rosta, T. Kalvas, R. Vendt, V. Allik, M. Noorma, ESTCube-1 in-orbit experience and lessons learned, IEEE Aerospace and Electronic Systems Magazine 30 (8) (2015) 12–22, doi: 10.1109/MAES.2015.150034.
[161] A. Kestilä, T. Tikka, P. Peitso, J. Rantanen, A. Näsilä, K. Nordling, H. Saari, R. Vainio, P. Janhunen, J. Praks, M. Hallikainen, Aalto-1 nanosatellite – technical description and mission objectives, Geoscientific Instrumentation, Methods and Data Systems 2 (2013) 121–130, doi: 10.5194/gi-2-121-2013.
[162] O. Khurshid, J. Selkäinaho, H. E. Soken, E. Kallio, A. Visala, Small satellite attitude determination during plasma brake deorbiting experiment, Acta Astronautica 129 (2016) 52–58, doi: 10.1016/j.actaastro.2016.08.035.
[163] J. Praks, M. R. Mughal, R. Vainio, P. Janhunen, J. Envall, P. Oleynik, A. Näsilä, H. Leppinen, P. Niemelä, A. Slavinskis, J. Gieseler, P. Toivanen, T. Tikka, T. Peltola, A. Bosser, G. Schwarzkopf, N. Jovanovic, B. Riwanto, A. Kestilä, A. Punkkinen, R. Punkkinen, H.-P. Hedman, T. Säntti, J.-O. Lill, J. M. K. Slotte, H. Kettunen, A. Virtanen, Aalto-1, multi-payload CubeSat: Design, integration and launch, Acta Astronautica 187 (2021) 370–383, doi: 10.1016/j.actaastro.2020.11.042.
[164] M. R. Mughal, J. Praks, R. Vainio, P. Janhunen, J. Envall, A. Näsilä, P. Oleynik, P. Niemelä, S. Nyman, A. Slavinskis, J. Gieseler, N. Jovanovic, B. Riwanto, P. Toivanen, H. Leppinen, T. Tikka, A. Punkkinen, R. Punkkinen, H.-P. Hedman, J.-O. Lill, J. M. K. Slotte, Aalto-1, multi-payload CubeSat: In-orbit results and lessons learned, Acta Astronautica 187 (2021) 557–568, doi: 10.1016/j.actaastro.2020.11.044.
[165] M. Palmroth, J. Praks, R. Vainio, P. Janhunen, E. K. J. Kilpua, A. Afanasiev, M. Ala-Lahti, A. Alho, T. Asikainen, E. Asvestari, M. Battarbee, A. Binios, A. Bosser, T. Brito, M. Dubart, J. Envall, U. Ganse, N. Y. Ganushkina, H. George, J. Gieseler, S. Good, M. Grandin, S. Haslam, H.-P. Hedman, H. Hietala, N. Jovanovic, S. Kakakhel, M. Kalliokoski, V. V. Kettunen, T. Koskela, E. Lumme, M. Meskanen, D. Morosan, M. R. Mughal, P. Niemelä, S. Nyman, P. Oleynik, A. Osmane, E. Palmerio, J. Peltonen, Y. Pfau-Kempf, J. Plosila, J. Polkko, S. Poluianov, J. Pomoell, D. Price, A. Punkkinen, R. Punkkinen, B. Riwanto, L. Salomaa, A. Slavinskis, T. Säntti, J. Tammi, H. Tenhunen, P. Toivanen, J. Tuominen, L. Turc, E. Valtonen, P. Virtanen, T. Westerlund, FORESAIL-1 cubesat mission to measure radiation belt losses and demonstrate deorbiting, Journal of Geophysical Research: Space Physics 124 (7) (2019) 5783–5799, doi: 10.1029/2018JA026354.